Comput Mech (2013) 52:1199–1219
DOI 10.1007/s00466-013-0872-5

ORIGINAL PAPER

A method of two-scale analysis with micro-macro decoupling scheme: application to hyperelastic composite materials

K. Terada · J. Kato · N. Hirayama · T. Inugai · K. Yamamoto

Received: 10 June 2012 / Accepted: 5 May 2013 / Published online: 21 May 2013

Abstract The aim of this study is to propose a strategy for performing nonlinear two-scale analysis for composite materials with periodic microstructures (unit cells), based on the assumption that a functional form of the macroscopic constitutive equation is available. In order to solve the two-scale boundary value problems (BVP) derived within the framework of the homogenization theory, we employ a class of the micro-macro decoupling scheme, in which a series of numerical material tests (NMTs) is conducted on the unit cell model to obtain the data used for the identification of the material parameters in the assumed constitutive model. For the NMTs with arbitrary patterns of macro-scale loading, we propose an extended system of the governing equations for the micro-scale BVP, which is equipped with the external material points or, in the FEM, control nodes. Taking an anisotropic hyperelastic constitutive model for fiber-reinforced composites as an example of the assumed macroscopic material behavior, we introduce a tensor-based method of parameter identification with the 'measured' data in the NMTs. Once the macro-scale material behavior is successfully fitted with the identified parameters, the macro-scale analysis can be performed, and, as may be necessary, the macro-scale deformation history at any point in the macro-structure can be applied to the unit cell to evaluate the actual micro-scale response.

K. Terada · J. Kato (✉) · T. Inugai
Department of Civil Engineering, Tohoku University, Aza-Aoba 6-6-06, Aramaki, Aoba-ku, Sendai 980-8579, Japan
e-mail: kato@irides.tohoku.ac.jp; tei@irides.tohoku.ac.jp

N. Hirayama
Fukushima Research Center, Nitto Boseki Co., Ltd., 20 Sakura Ipponsugi, Fukushima 960-2154, Japan

K. Yamamoto
Cybernet Systems Co.,Ltd., Kanda-neribeicho, Chiyoda-ku, Tokyo 101-0022, Japan

Keywords Two-scale analysis · Micro-macro decoupling scheme · Numerical material testing · Homogenization · Anisotropic hyperelasticity

1 Introduction

The mathematical theory of homogenization [1–3] has been recognized as a rigorous modeling methodology for characterizing the macro-scale mechanical behavior of heterogeneous media with periodic microstructures, often called unit cells. The so-called localization capability in the theory [4], which provides clear distinction from the classical or theoretical counterparts in engineering science [5], is an appealing feature to researchers in the area of computational mechanics, since it enables us to compute the actual microscopic stress and strain in a unit cell with the help of the finite element method (FEM). A series of work done by Léné and his co-workers [6,7] was probably one of the earliest developments in this context. It is, however, no exaggeration to say that Guedes and Kikuchi [8] had a head start on the full-fledged research activities with a view to the applications of the homogenization and localization capabilities in engineering practice, and their work was followed by a string of developments, too numerous to comprehensively list here. But, this much can be safely said—the main interest has centered on the characterization of the macro-scale nonlinear mechanical behavior of composite materials or heterogeneous solids by solving the micro-scale boundary value problem (BVP).

The micro- and macro-scale governing equations derived for nonlinear homogenization problems in solid mechanics, which define the so-called two-scale BVP, are essentially the same as those in linear problems. However, the major difference between the linear and nonlinear homogenization problems is that the former provides us with the functional form of the linear macroscopic constitutive model, whose material parameters are evaluated by a series of *numerical material tests* (NMTs), while the latter does not. In the linear problem, the NMTs 'measure' the fundamental material responses at the macro-scale so that the homogenized material properties can be identified, and their micro-scale counterparts, called the characteristic functions, are obtained by solving the corresponding micro-scale BVP. The introduction of the characteristic functions enables us to decouple the micro- and macro-scale variables and, therefore, prevents us from solving as many micro-scale problems at the macroscopic material points in response to the macro-scale strains there; see e.g., [2,8] for a lucid explanation.

On the other hand, nonlinear homogenization neither provides an explicit form of the macroscopic constitutive equation, nor allows us to separate the micro- and macro-scale variables. As a result, the micro-scale BVP must be solved with the macroscopic strain field as datum to evaluate the corresponding macroscopic stress at a material point of the macro-structure. Due to this inconvenience, many previous studies have been entirely focused on the characterization of the *local* material behavior by solving a single micro-scale problem under certain assumed patterns of the macroscopic loading; see for example, References [9–12] for applications of elastic-plastic behavior and [13–15] for micro-scale damage-induced inelastic behavior of heterogeneous solids. The main purpose of these studies is to illustrate the macroscopic material characteristics by solving the micro-scale BVP for their own unit cells, but the solution of the macro-scale BVP has received little attention.

To obtain the solution of the macro-scale BVP within the framework of the nonlinear homogenization, Terada and Kikuchi [16] demonstrated the two-scale (or global-local) computations for elastic-plastic deformations of fiber-reinforces composites, in which the micro- and macro-scale BVPs are completely coupled. More specifically, a unit cell's FE model is assigned to each integration point in the macro-scale FE model, and the solutions of the macro-scale BVP, such as the macroscopic stress and strain, are the volume average of the corresponding solution of the micro-scale BVP. Independently, or inspired by this attempt, several studies have been done on the development of a *micro–macro coupling scheme* for two-scale analyses; see, e.g. [17–21]. This scheme appears to be robust: it is applicable to various types of macroscopic nonlinear material behavior even in cases where their macroscopic constitutive equations are unknown. In fact, this approach seems to be the only way to evaluate the nonlinear macroscopic material response of a heterogeneous medium when the analytical expression of its macroscopic constitutive relation is hard to formulate; see e.g., References [22,23].

However, as readily understood from the nature of the micro-macro coupling scheme, in which a nonlinear micro-scale FE analysis must be conducted for a unit cell to obtain the macroscopic stress at a single integration point, the computational costs required in executing the fully two-scale (or global-local) computations are very large indeed [16,21]. Thus, the application of the coupling scheme to practical problems is not feasible without some sort of countermeasure. In fact, there have been some attempts to improve the computational efficiency of the coupling algorithm; see for example, Yamada [24] who introduced the block Newton–Raphson method to solve the two-scale BVP. A more direct approach to reduce the computational cost would be to utilize a distributed memory parallel computer [29], with each processor taking charge of the micro-scale computation. It seems, however, to be difficult to implement these methods for the coupling scheme into existing general-purpose FEM software, since micro- and macro-scale FE models involve a single two-scale computation.

Other approaches based on the model reduction techniques are worth mentioning, which enable us to reduce macroscopic internal variables for inelastic homogenization procedures; see e.g., [25,26]. In this context, Oskay and Fish [28] proposed an approximate method to reduce the model size for the micro-scale problems with the help of the transformation field analysis. The methods are followed by Yvonnet and He [27] with the help of the proper orthogonal decomposition, which are utilized to construct the macroscopic constitutive database as mentioned below.

For this reason, we expect from a viewpoint of practical use that the alternative approach to resolve the problems mentioned above is developed. With our eyes set on the philosophy of computer-aided engineering (CAE) in this context, the utility value of the two-scale analysis method based on homogenization can be enhanced in practice by the micro–macro *decoupling* scheme. In this context, Terada and Kikuchi [16], who considered the practical applications while developing their coupling scheme, proposed the idea of a constitutive database to decouple the micro- and macro-scale BVPs. In their approach, the data of the discrete macroscopic stress responses are obtained beforehand in the macroscopic strain space by conducting a series of NMTs, and are stored into a database file, which the evaluations of the actual macro-scale stress in the macro-scale analysis use to make interpolations within the strain spaces. This approach has been followed by some authors to deal with nonlinear elastic deformations [30,31], but seems not to be feasible in the case of general inelastic deformations. Thus, more reliable and efficient means must be developed to put the homogenization-based method for two-scale analyses to practical use.

In this paper, we propose a strategy of conducting nonlinear two-scale analyses of composite materials with periodic microstructures (unit cells) by applying a class of the micro-macro decoupling scheme [32] to solve the two-scale BVP, which can be derived within the framework of the homogenization theory. The suggested scheme strongly relies on the method of numerical material testing, which corresponds to the homogenization process for the unit cells, just like the computational homogenization method for linear problems. To be more specific, assuming the concrete functional form of the macro-scopic constitutive model, we conduct a series of NMTs on the *numerical specimen*, i.e., the unit cell's FE model, to obtain the nonlinear macro-scale material behavior. By means of the 'measured' data in the NMTs, the material parameters in the assumed constitutive model are identified with an appropriate method of parameter identification. Once the macro-scale material behavior is successfully fitted with the identified parameters, the macro-scale analysis can be performed, and, as may be necessary, the macro-scale deformation history at any point in the macro-structure can be applied to the unit cell to evaluate the actual micro-scale response. In this paper, an anisotropic hyperelastic constitutive model for fiber-reinforced composites is taken as a simple and lucid example to demonstrate the proposed method. A similar, but essentially different study has been reported by Ren et al. [33], which proposed a continuum damage model that accounts for the micro-crack evolutions with the help of numerical material testing concept. Although the inelastic and brittle damage behavior due to micro-cracking can successfully be represented by the proposed model, neither the micro–macro consistency within the framework of mathematical homogenization has been examined by comparing the macroscopic constitutive responses with those obtained by the microscopic analyses, nor the extended system for the microscopic problem is utilized with an intention to implement the model into the general-purpose software.

An outline of this paper is as follows. In Sect. 2, we start out by providing the two-scale BVP for general finite deformation problems and then introduce a decoupling scheme to solve the micro- and macro-scale BVPs. Section 3 is devoted to detailed explanations of the numerical material testing suggested as a process in our scheme. Here, the extended system for the micro-scale BVP with the periodic boundary condition is formulated by introducing external material points, whose counterparts in the FEM are referred to as the *control nodes* in this study, so that any pattern of macroscopic stress and deformation can be applied to the unit cell models. It is to be noted that, thanks to the introduction of the *control nodes* located outside the unit cell model, the corresponding micro-scale analyses can be conducted by general-purpose FEM software available in the market. In Sect. 4, employing an anisotropic hyperelastic constitutive model to represent the macroscopic material behavior of fiber-reinforced composites, a tensor-based method of parameter identification for the model is provided. In Sect. 5, we illustrate the train of numerical analyses involved in the proposed strategy of two-scale analyses for fiber-reinforced composites. The numerical examples demonstrate that the proposed approach is expected to be eligible for both the micro- and macro-scale CAE systems, since the micro- and macro-scale numerical analyses are completely decoupled, yet are related to each other with regard to the adequacy of the assumed constitutive model.

2 Two-scale analysis based on homogenization theory

In the multiscale mathematical modeling for composite materials with periodic microstructures (unit cells) by means of the homogenization theory [1–3], micro- and macroscopic boundary-value problems (BVP) are separately derived, and the resulting set of BVPs is referred to as a two-scale BVP [21,34]. In this section, after presenting the individual sets of micro- and macroscopic governing equations that define the two-scale BVP, we describe the micro-macro decoupling scheme to perform the corresponding two-scale analysis.

2.1 Two-scale boundary-value problem

With reference to Fig. 1, we provide the two-scale BVP for a composite material with unit cells. The formulation here is made consistently within the framework of finite strain theory [34].

To measure the microscopic mechanical behavior of a unit cell, the spatial position $\boldsymbol{Y}$ in the micro-scale initial or reference configuration $\mathcal{Y}_0$ of the unit cell domain and the spatial position $\boldsymbol{y}$ in the micro-scale current configuration $\mathcal{Y}$ are introduced. They are inter-related by the micro-scale motion as $\boldsymbol{y} = \varphi(\boldsymbol{Y}) = \boldsymbol{Y} + \boldsymbol{w}(\boldsymbol{Y})$, where $\boldsymbol{w}$ is the micro-scale displacement of the unit cell. Then the micro-scale deformation gradient is defined as

$$\begin{aligned}\boldsymbol{F} = \nabla_Y \varphi(\boldsymbol{X};\boldsymbol{Y}) &= \nabla_Y \boldsymbol{w}(\boldsymbol{X};\boldsymbol{Y}) + \boldsymbol{1}\\ &= \tilde{\boldsymbol{H}}(\boldsymbol{X}) + \nabla_Y \boldsymbol{u}^*(\boldsymbol{X};\boldsymbol{Y}) + \boldsymbol{1},\end{aligned} \tag{1}$$

where $\boldsymbol{X}$ denotes the macroscopic material point in the macro-scale reference configuration, but is not an independent variable in the micro-scale kinematics. Here, ∇_Y is the gradient operator with respect to the micro-scale $\boldsymbol{Y}$, $\tilde{\boldsymbol{H}}$ is the macroscopic displacement gradient that is independent of $\boldsymbol{Y}$, $\boldsymbol{1}$ is the second-order identity tensor, and $\boldsymbol{u}^*$ is the Y-periodic displacement field that represents a fluctuation due to micro-scale heterogeneity. The fluctuation displacement $\boldsymbol{u}^*$ in (1) is assumed to be subjected to the periodic boundary condition on the unit cell's external boundary $\partial\mathcal{Y}_0$ as follows:

$$\boldsymbol{u}^*\big|_{\partial\mathcal{Y}_0^{[J]}} = \boldsymbol{u}^*\big|_{\partial\mathcal{Y}_0^{[-J]}} \quad (J = 1,\ 2,\ 3), \tag{2}$$

where $\partial\mathcal{Y}_0^{[\pm J]}$ indicates a pair of opposite external boundaries of the unit cell [4]. This condition is referred to as the Y-periodicity in the theory. It is assumed that a unit cell is a rectangular parallelepiped-shape, and its external boundaries are arranged parallel to the three micro-scale coordi-

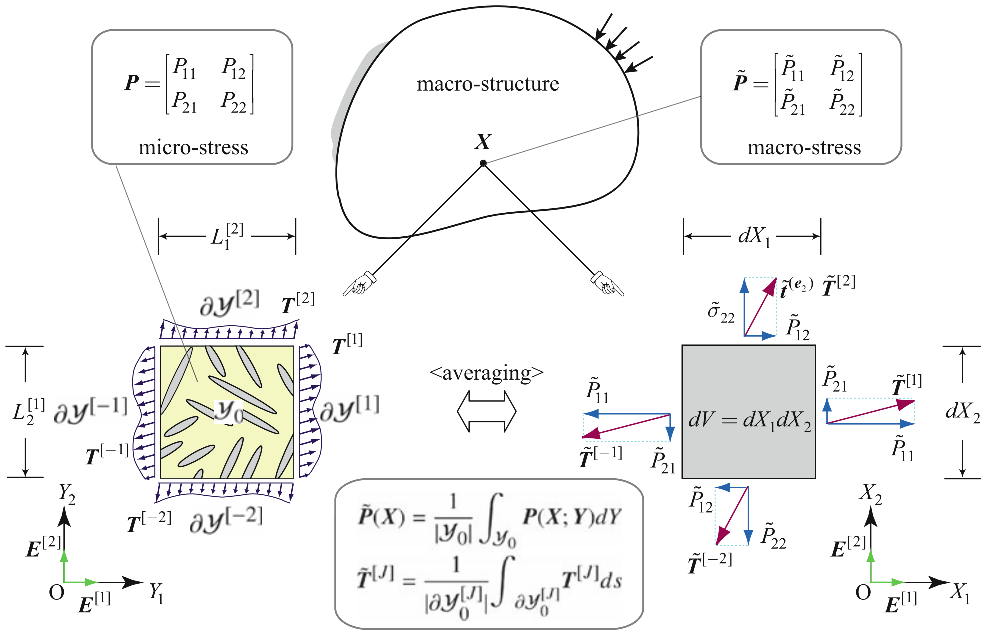

Fig. 1 Concept of numerical material testing based on homogenization method (in 2D).

nate planes Y_J so that the basis vector $\boldsymbol{E}^{[J]}$ is an outward unit normal vector on $\partial\mathcal{Y}_0^{[J]}$ in the initial configuration.

The micro-scale self-equilibrium equation for the unit cell is given as

$$\nabla_Y \cdot \boldsymbol{P} = \boldsymbol{0} \quad \text{in} \quad \mathcal{Y}_0, \tag{3}$$

where $\boldsymbol{P}$ is the micro-scale 1st-Piola–Kirchhoff (PK) or nominal stress. The micro-scale governing equation is completed by the introduction of a relevant constitutive model as a function of the micro-scale deformation gradient $\boldsymbol{F}$ defined by (1), and possibly other micro-scale internal state variables in the case of inelastic materials. Although arbitrary constitutive models are acceptable for the micro-scale stress response in this framework, we take a class of hyperelastic models in this study so that the corresponding macroscopic constitutive model could be an anisotropic hyperelastic one.

Owing to the Y-periodicity, the Piola traction vector $\boldsymbol{T}^{(N)} = \boldsymbol{P} \cdot \boldsymbol{N}$, with $\boldsymbol{N}$ being the outward unit normal vector on the corresponding surface, satisfies the following anti-periodicity conditions on the unit cell boundary $\partial\mathcal{Y}_0$ in the initial configuration:

$$\boldsymbol{T}^{[J]} + \boldsymbol{T}^{[-J]} = \boldsymbol{0}, \tag{4}$$

where we have defined $\boldsymbol{T}^{[\pm J]} := \boldsymbol{T}^{(\pm \boldsymbol{E}^{[J]})}$ with $\boldsymbol{E}^{[J]}$ being the basis vector of the Y_J-axis.

On the other hand, denoting the macro-scale reference and current configurations by $\mathcal{B}_0$ and $\mathcal{B}$, respectively, and the macro-scale initial position by $\boldsymbol{X} \in \mathcal{B}_0$, we have its current position by the macro-scale motion $\boldsymbol{x} = \tilde{\varphi}(\boldsymbol{X}) \in \mathcal{B}$, and we can define the macro-scale deformation gradient as $\tilde{\boldsymbol{F}} = \nabla_X \tilde{\varphi}$ with ∇_X being the gradient operator with respect to the macro-scale $\boldsymbol{X}$. At the same time, $\tilde{\boldsymbol{F}}$ is defined as the volume average of the corresponding micro-scale deformation gradient over the unit cell as

$$\tilde{\boldsymbol{F}} = \frac{1}{|\mathcal{Y}_0|} \int_{\mathcal{Y}_0} \boldsymbol{F} dY = \tilde{\boldsymbol{H}} + \boldsymbol{1}, \tag{5}$$

where $|\mathcal{Y}_0|$ is the initial volume of the unit cell. Here, this relationship is derivable from (1) along with the Y-periodicity of the fluctuation displacement $\boldsymbol{u}^*$, and the macro-scale displacement gradient can be identified with $\tilde{\boldsymbol{H}} = \nabla_X \tilde{\boldsymbol{u}}(\boldsymbol{X})$, with $\tilde{\boldsymbol{u}}$ being the macro-scale displacement field. Similarly, the macro-scale 1st PK stress can be defined as the volume average of the corresponding micro-scale stress over the unit cell as.

$$\tilde{\boldsymbol{P}} = \frac{1}{|\mathcal{Y}_0|} \int_{\mathcal{Y}_0} \boldsymbol{P} dY, \tag{6}$$

which satisfies the following macro-scale equilibrium equation:

$$\nabla_X \cdot \tilde{\boldsymbol{P}} + \tilde{\boldsymbol{b}} = \boldsymbol{0} \quad \text{in} \quad \mathcal{B}_0, \tag{7}$$

where $\tilde{\boldsymbol{b}}$ is the body force. It is well known that the nonlinear homogenization theory does not have a logic that accommodates the explicit form of the macroscopic constitutive equation, but it allows us to use (6) to evaluate the macroscopic stress $\tilde{\boldsymbol{P}}$ after solving the micro-scale problem for the equilibrated micro-scale stress $\boldsymbol{P}$.

In summary, the micro-scale BVP is to be solved for the set of solutions $\boldsymbol{w}$, $\boldsymbol{F}$, $\boldsymbol{P}$ that satisfies the micro-scale equilibrium equation (3) along with the kinematic condition (1) and a relevant constitutive equation, while the macro-scale BVP is for $\tilde{\boldsymbol{u}}$, $\tilde{\boldsymbol{F}}$, $\tilde{\boldsymbol{P}}$ that satisfies (5), (6) and (7). It is noted that the micro-scale BVP can be solved only if the macro-scale solution is given and vice versa. The BVP composed of the micro- and macro-scale BVPs is called the two-scale BVP in the mathematical homogenization theory.

2.2 Micro–macro coupling and decoupling schemes for the two-scale BVP

In the two-scale BVP, the macroscopic constitutive equation is an implicit function of the solutions of the micro-scale BVP and, thus, the micro-scale BVP indirectly represents the macroscopic material response. That is, it is not until the micro-scale equilibrated stress is determined that the macroscopic stress can be calculated in view of (6). Therefore, if the two-scale coupling analysis is performed by the FEM, the micro-scale BVP must be associated with an integration point located in a macro-scale finite element model and solved for the micro-scale equilibrated stress to evaluate the macro-scale stress by the averaging relation (6), which must satisfy the macro-scale BVP at the same time. In particular, when an implicit and incremental solution method with a Newton-Raphson type iterative procedure is employed to solve the two-scale BVP, the micro-scale BVP is to be solved in every iteration to attain the macro-scale equilibrium state at every loading step. Needless to say, the micro-scale BVP is also nonlinear and therefore requires the iterative method. This type of solution scheme to solve the two-scale BVP is referred to as the micro-macro (or global-local) coupling scheme and is typified in [16,21,34].

The micro-macro coupling scheme is promising in the sense that almost all of the various types of macroscopic material behavior can be captured without knowing their explicit functional forms of material models if the unit cell is eligible for a RVE. However, the nature of the method means it requires a significant amount of computational cost. In fact, the model size of the macro-scale BVP raises the number of micro-scale BVPs to the second power, since each macro-scale integration point is associated with its own micro-scale BVP. Although some parallel algorithms can reduce the cost to some extent [29], we are bound to say that the coupling scheme is all but useless in most practical applications. Therefore, the decoupling of micro- and macro-scale BVPs is indispensable for applying the two-scale approach based on homogenization to various problems encountered in practice [32].

The precondition of decoupling is that we are able to pick up a constitutive model to properly characterize the macroscopic material behavior that would be obtained from the numerical analysis on the micro-scale BVP. It is noted that, from a practical point of view, approximated constitutive models allow alternatives, since there might not be a rigorous model available depending on the type of composite materials. Once the functional form of an appropriate macroscopic constitutive equation is assumed, several micro-scale numerical analyses are performed on the unit cell to obtain its material parameters. The set of micro-scale analyses for this purpose can be referred to as numerical material testing (NMT), an essential process of the micro-macro decoupling scheme [32]. The concrete procedure of the method is described as follows:

(i) An appropriate constitutive model relevant for the macroscopic material behavior under consideration is assumed.
(ii) A series of NMTs is conducted on a unit cell model (FE mesh), which is regarded as a ‘numerical specimen’, to obtain the homogenized or macroscopic material behavior. Note that the loading patterns here hinge on the selected constitutive model.
(iii) Material parameters of the assumed constitutive model are identified by means of the ‘empirical’ data obtained from the NMTs and an appropriate curve fitting scheme.
(iv) FE analyses are carried out to solve the macro-scale BVP using the assumed constitutive model with identified material parameters.
(v) If necessary, after extracting the time-series of macroscopic deformation history from the macroscopic analysis result and applying it as a series of boundary conditions, the localization analyses are performed to evaluate what has actually been happening inside the unit cell during the macroscopic deformation process.

Since the material models used in unit cells are supposed to be given in the computational homogenization method, the homogenized or macroscopic material model to be assumed in Step (i) is expected to partially inherit the micro-scale material behavior. For example, if the unit cell model of a fiber-reinforced plastic is assumed to be composed of isotropic hyperelastic materials, the corresponding macroscopic material behavior can be anisotropic hyperelastic. Likewise, if the constituents are elastic-plastic materials, the macroscopic constitutive model should be within the scope of anisotropic plasticity. Even though micro-scale cracking is taken into account as in [23], the corresponding macroscopic material behavior may be represented by the anisotropic damage model approximately. However, assumed macroscopic constitutive models do not always properly represent the macroscopic material behavior properly, the decoupling scheme is just an approximate scheme. Thus, two-scale analysts are responsible for the degree of approximation, but the coupling scheme can be used rather than the decoupling one, if the highest level of accuracy is desired irrespective of computational costs.

3 A method of numerical material testing

Assuming that an appropriate constitutive model is found for the macroscopic nonlinear material behavior, we are concerned with the accuracy and validity of the NMT as part of the two-scale analysis. Given the macroscopic stress or deformation as a datum, the micro-scale BVP has to be solved for the micro-scale stress. Then, using (5) and (6), we obtain discrete macroscopic stress–strain curves, which can be regarded as 'experimental results'. In this section, we first introduce an extended system of the micro-scale BVP so that the arbitrary patterns of macroscopic loading are utilizable in the NMTs, and provide the concrete procedure of the NMT by using the standard FEM.

3.1 Alternative form of the micro-scale BVP

The integration of (1) with respect to $\boldsymbol{Y}$ yields the following form of the micro-scale displacement $\boldsymbol{w}$ of the unit cell:

$$\boldsymbol{w}(\boldsymbol{X};\boldsymbol{Y}) = \tilde{\boldsymbol{H}}(\boldsymbol{X})\cdot\boldsymbol{Y} + \boldsymbol{u}^*(\boldsymbol{X};\boldsymbol{Y}) + \boldsymbol{c}(\boldsymbol{X}), \tag{8}$$

where $\boldsymbol{c}$ is a constant vector independent of $\boldsymbol{Y}$. By substituting this expression into (2) that impose the Y-peridocity of the fluctuation displacement field, we have the constraint condition as

$$\boldsymbol{w}^{[J]} - \boldsymbol{w}^{[-J]} = \tilde{\boldsymbol{H}}\cdot\boldsymbol{L}^{[J]}, \tag{9}$$

where $\boldsymbol{w}^{[\pm k]} := \boldsymbol{w}|_{\partial\mathcal{Y}_0^{[\pm k]}}$. Here, we have defined the vector connecting the material points of a Y-periodicity pair as follows:

$$\boldsymbol{L}^{[J]} := \boldsymbol{Y}|_{\partial\mathcal{Y}_0^{[J]}} - \boldsymbol{Y}|_{\partial\mathcal{Y}_0^{[-J]}}, \tag{10}$$

which can be called the *side vector* of a unit cell.

Owing to the anti-periodicity of the Piola traction vector (4), the following relatiohship can be derived:

$$\tilde{\boldsymbol{T}}^{[J]} = \tilde{\boldsymbol{P}}\cdot\boldsymbol{E}^{[J]} = \frac{1}{|\partial\mathcal{Y}_0|}\int_{\partial\mathcal{Y}_0} \boldsymbol{P}\cdot\boldsymbol{E}^{[J]}dY = \frac{1}{|\partial\mathcal{Y}_0^{[J]}|}\int_{\partial\mathcal{Y}_0^{[J]}} \boldsymbol{T}^{[J]}ds, \tag{11}$$

where $|\partial\mathcal{Y}_0^{[J]}|$ is the area of the unit cell boundary $\partial\mathcal{Y}_0^{[J]}$. Also, denoting the spatial basis vector by $\boldsymbol{e}^{[i]}$, the components of $\tilde{\boldsymbol{P}}$ in (11) can be expressed as

$$\tilde{T}_i^{[J]} = \tilde{P}_{iJ} = \boldsymbol{e}^{[i]}\cdot(\tilde{\boldsymbol{P}}\cdot\boldsymbol{E}^{[J]}) = \frac{1}{|\partial\mathcal{Y}_0^{[J]}|}\int_{\partial\mathcal{Y}_0^{[J]}} T_i^{[J]}ds. \tag{12}$$

That is, the iJ-component of the macro-scale 1st PK stress, $\tilde{P}_{iJ}$, is the area average of the corresponding micro-scale Piola traction vector, $T_i^{[J]}$, at the unit cell boundary $\partial\mathcal{Y}_0^{[J]}$. Therefore, the area average of the anti-periodicity condition (4) for the micro-scale Piola traction vector is nothing but the action and reaction law of the macro-scale Piola traction vector on the macro-scale surface whose outward unit normal vector coincides with $\boldsymbol{E}^{[J]}$. The proof of Eq. (11), or equivalently (12), is provided in Appendix A.

When the response function of the micro-scale 1st PK stress $\mathcal{F}(\boldsymbol{F})$ is assumed for a material model used in the unit cell, the micro-scale BVP is given anew as

$$\left.\begin{array}{l}\nabla_Y\cdot\boldsymbol{P} = \boldsymbol{0}\\ \boldsymbol{F} = \nabla_Y\boldsymbol{w} + \boldsymbol{1}\\ \boldsymbol{P} = \mathcal{F}(\boldsymbol{F})\end{array}\right\}\ \text{in }\mathcal{Y}_0, \tag{13}$$

$$\left.\begin{array}{l}\boldsymbol{w}^{[J]} - \boldsymbol{w}^{[-J]} = \tilde{\boldsymbol{H}}\cdot\boldsymbol{L}^{[J]}\\ \quad\text{and}\\ \tilde{\boldsymbol{T}}^{[J]} = \dfrac{1}{|\partial\mathcal{Y}_0^{[J]}|}\displaystyle\int_{\partial\mathcal{Y}_0^{[J]}}\boldsymbol{P}\cdot\boldsymbol{E}^{[J]}ds\end{array}\right\}\ \text{on }\partial\mathcal{Y}_0^{[J]}. \tag{14}$$

The data to be prepared for this BVP are the macro-scale deformation (e.g. $\tilde{\boldsymbol{H}}$) and/or the macroscopic stress (e.g. $\tilde{\boldsymbol{P}}$) in addition to the information about the unit cell's geometry and the material models for constituents with relevant properties. It is realized that this BVP is a standard qausi-static equilibrium problem except that the displacement constraints and the loading conditions at the boundaries are somewhat special. As will be seen later, since the 9 components of the macro-scale displacement gradient $\tilde{\boldsymbol{H}}$ and the 9 components of the micro-scale 1st PK stress $\tilde{\boldsymbol{P}}$ are dual, they cannot be given independently.

3.2 Extended system of the micro-scale BVP with external material points

We here introduce an *extended system* of the micro-scale BVP by introducing fictitious material points located outside the unit cell domain. Although these additional points can be inside the unit cell, we call them 'external' material points in this study.

The constraint condition (9), or equivalently the first equation in (14), can be re-written as

$$\boldsymbol{w}^{[J]} - \boldsymbol{w}^{[-J]} = \boldsymbol{q}^{[J]}, \tag{15}$$

where we have defined the relative displacement vectors as

$$\boldsymbol{q}^{[J]} := \tilde{\boldsymbol{H}}\cdot\boldsymbol{L}^{[J]}. \tag{16}$$

Corresponding to the three pairs of the unit cell boundary surfaces $\partial\mathcal{Y}_0^{[\pm J]}$, we introduce three external material points, to which the degrees-of-freedom (DOFs) of the three relative displacement vectors $\boldsymbol{q}^{[J]}$ in (16) are assigned as depicted in Fig. 2. Thus, the resulting extended system of the governing equations for a unit cell has nine more DOFs than the origianl one (13) with (14) in a 3D setting.

Owing to the introduction of the external material points, Eq. (15) is regarded as a three-point constraint equation that

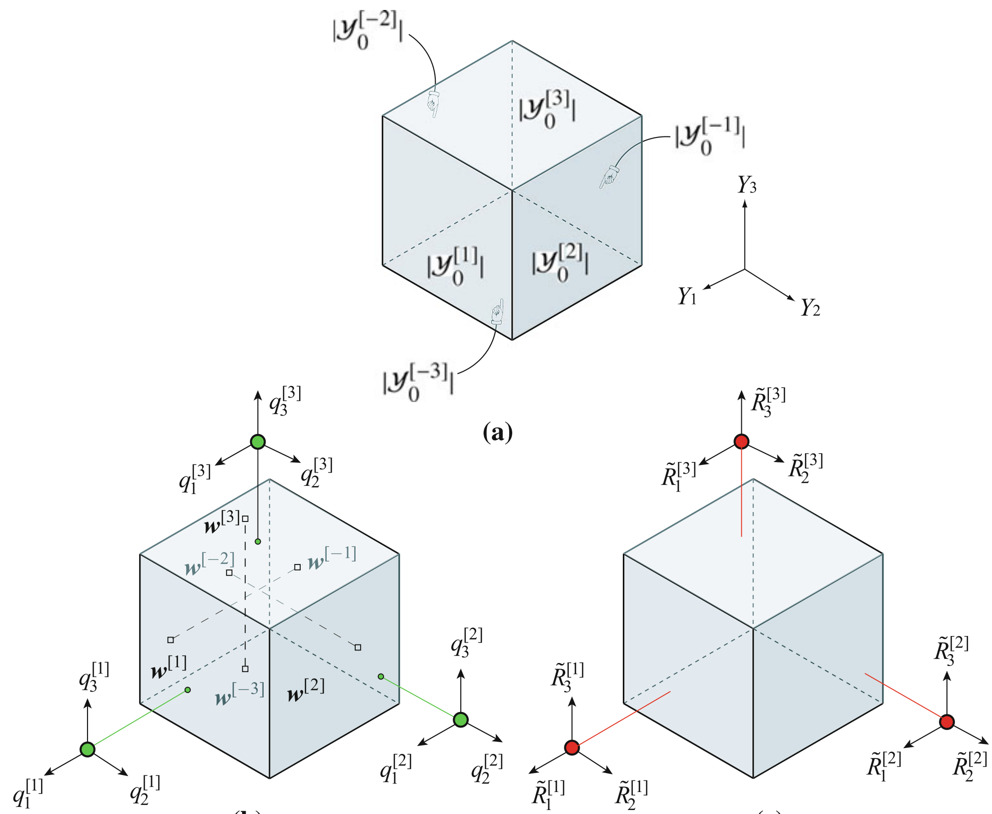

Fig. 2 External material points for controlling relative displacements and reaction forces on unit cell' boundary surfaces: **a** boundary surfaces; **b** relative displacements; **c** reaction forces.

relates the displacement vectors of an arbitrary pair of material points on the boundary surface $\partial\mathcal{Y}_0^{[\pm J]}$ to the relative displacement vector of the corresponding single external point, while eqn. (9) is regarded as a two-point constraint condition with $\boldsymbol{q}^{[J]}$ as a constant vector. As will seen later, this feature is not only of particular convenience when evaluating the macroscopic stress and strain, but also the only way to impose the macroscopic stress components directly to the unit cell without solving the macroscopic BVP (7).

For instance, if we solve the micro-scale equilibrium equation (3) for a unit cell by specifying the i-th component of the displacement $q_i^{[J]}$ at an external point, not only the micro-scale stress and strain fields, but also the i-th component of the reaction force $\tilde{R}_i^{[J]}$ at the external point should be obtained. We then note that this reaction force $\tilde{R}_i^{[J]}$ can be identified with the area integral of the micro-scale Piola traction vector $T_i^{[J]}$ over $\partial\mathcal{Y}_0^{[J]}$, which is associated with the constraint condition (15) for the relative displacement $w_i^{[J]} - w_i^{[-J]}$. That is, we have

$$\tilde{R}_i^{[J]} = \int_{\partial\mathcal{Y}_0^{[J]}} T_i^{[J]} ds, \tag{17}$$

from which the corresponding component of the macro-scale Piola traction vector can be obtained as

$$\tilde{P}_{iJ} = \tilde{T}_i^{[J]} = \frac{\tilde{R}_i^{[J]}}{|\partial\mathcal{Y}_0^{[J]}|}. \tag{18}$$

Therefore, once all the resultant forces acting on the three external material points are evaluated, all the components of the macro-scale stress can be obtained.

On another front, the specification of the components of a resultant force $\tilde{R}_i^{[J]}$ to an external point is possible, and implies that the components of the macroscopic stress $\tilde{P}_{iJ}$ can be imposed on a unit cell irrespective of the corresponding macro-scale problem. In this case, the component of the displacement $q_i^{[J]}$ is unknown, but can be translated to the component of the macro-scale displacement $\tilde{H}_{iK} L_K^{[J]}$ by means of (16).

In the mathematical theory of homogenization, a unit cell *domain* is identified with a single macroscopic material *point*. This means that each macroscopic field variable is determined from a single unit cell. In this context, the three external points have nine DOFs in total, which are the same in number as the independent components of the macro-scale 1st PK stress or of the macro-scale displacement gradient.

Therefore, the set of components of the macroscopic stress $\tilde{\boldsymbol{P}}$ is uniquely associated with the set of components of the reaction force $\tilde{\boldsymbol{R}}$ at the three external material points. Also, the displacement gradient $\tilde{\boldsymbol{H}}$ is uniquely related to the relative displacement $\boldsymbol{q}^{[J]}$. Thus, these external material points enable us to evaluate the macroscopic quantities without using the corresponding microscopic quantities. This feature is of particular advantage especially when the numerical material testing is conducted with commercial FEM-software, as explained below.

3.3 Finite element analysis for a unit cell with external material points

We here explain the usage of the external material points to solve the micro-scale BVP with a view to utilizing a general-purpose FEM code available on the market. For the sake of simplicity, only a rectangular parallelepipe-shaped unit cell is considered, and its sides are assumed to be parallel to one of the micro-scale coordinate planes so that only the J-th component of the side vector $\boldsymbol{L}^{[J]}$ is non-zero.

For preparation of the finite element analysis (FEA) for the micro-scale BVP, the spatial domain of the unit cell is discretized to generate its FE mesh. At the same time, each external material point is also 'discretized' to an element with a single node which has three DOFs and no mass. Since the external material points enables us to control the components of the macro-scale stress and deformation, as explained above, the node corresponding to an external material point is referred to as a *control node* in this study. Thus, we obtain an *extended system* of FE-discretized equations involving nine additional DOFs of three control nodes. In the following, we introduce some specific usages of the three control nodes to solve the extended system.

First, the macro-scale deformation is assumed to be known; that is, all the components of the macroscopic displacement gradient $\tilde{\boldsymbol{H}}$ are given as data. Using (16), we obtain all the components of the nodal displacement vector $\boldsymbol{q}^{[J]}$ at the three control nodes located on the unit cell boundary $\partial\mathcal{Y}_0^{[J]}$ $(J = 1, \ , 2, \ 3)$. Then, given all the components $q_i^{[J]}$, we solve the extended system of FE equations for the micro-scale BVP (13) with the nine sets of 'two-point' constraints realized by (15). The results of the FEA contain not only the micro-scale displacement, strain and stress, but also the reaction force $\boldsymbol{R}^{[J]}$. Therefore, the macro-scale 1st PK stress $\tilde{\boldsymbol{P}}$ can be computed from (18), without performing a numerical integration on (6). Also, since the macro-scale displacement gradient $\tilde{\boldsymbol{H}}$ has been given as a datum, the macro-scale deformation gradient can be computed as $\tilde{\boldsymbol{F}} = \boldsymbol{1} + \tilde{\boldsymbol{H}}$ and in turn its determinant $\tilde{J} = \det\tilde{\boldsymbol{F}}$ so that the macro-scale true (Cauchy) stress is computed as $\tilde{\boldsymbol{\sigma}} = \tilde{\boldsymbol{P}}\tilde{\boldsymbol{F}}^{\mathrm{T}}/\tilde{J}$

Secondly, let us suppose that the macro-scale stress is known; that is, all the components of the macro-scale 1st PK stress $\tilde{\boldsymbol{P}}$ are given as data. All the components of the resultant force vector $\tilde{R}_i^{[J]}$ at the three control nodes are determined by means of (18). In this case, all the components of the nodal displacement vector $\boldsymbol{q}^{[J]}$ are unknown in the extended system of FE equations for the unit cell. Once the solution of the system is obtained, we can obtain the following relationship:

$$\boldsymbol{Q} = \tilde{\boldsymbol{H}} \cdot \boldsymbol{L}, \tag{19}$$

from which the macro-scale displacement gradient can be evaluated as $\tilde{\boldsymbol{H}} = \boldsymbol{Q} \cdot \boldsymbol{L}^{-1}$. Here, we have defined $\boldsymbol{Q}$ as the matrix composed of three sets of the displacement vectors $\boldsymbol{q}^{[J]}$ at the control nodes and $\boldsymbol{L}^{[J]}$ $(J = 1, \ , 2, \ 3)$ as the matrix composed of the side vectors. To be more presice, they are respectively defined as

$$\boldsymbol{Q} = \left[\boldsymbol{q}^{[1]}\,\boldsymbol{q}^{[2]}\,\boldsymbol{q}^{[3]}\right] \quad \text{and} \quad \boldsymbol{L} = \left[\boldsymbol{L}^{[1]}\,\boldsymbol{L}^{[2]}\,\boldsymbol{L}^{[3]}\right]. \tag{20}$$

The computation of the macro-scale deformation gradient $\tilde{\boldsymbol{F}} = \boldsymbol{1} + \tilde{\boldsymbol{H}}$ is straightforward and is followed by the evaluation of the macro-scale right- and left-Cauchy-Green (CG) deformation tensors as, respectively, $\tilde{\boldsymbol{C}} = \tilde{\boldsymbol{F}}^{\mathrm{T}}\tilde{\boldsymbol{F}}$ and $\tilde{\boldsymbol{b}} = \tilde{\boldsymbol{F}}\tilde{\boldsymbol{F}}^{\mathrm{T}}$. Furthermore, we denote the eigenvalues of the macro-scale right- and left-stretch tensors $\tilde{\boldsymbol{U}}$ and $\tilde{\boldsymbol{V}}$ by $\tilde{\lambda}_\alpha$, and the corresponding eigenvectors by $\boldsymbol{N}_\alpha$ and $\boldsymbol{n}_\alpha$, respectively. Then, the spectral decomposition of $\tilde{\boldsymbol{C}}$ and $\tilde{\boldsymbol{b}}$ are respectively given as follows:

$$\tilde{\boldsymbol{C}} = \sum_{\alpha=1}^{3} \tilde{\lambda}_\alpha^2 \boldsymbol{N}_\alpha \otimes \boldsymbol{N}_\alpha, \quad \text{and} \quad \tilde{\boldsymbol{b}} = \sum_{\alpha=1}^{3} \tilde{\lambda}_\alpha^2 \boldsymbol{n}_\alpha \otimes \boldsymbol{n}_\alpha, \tag{21}$$

from which the material and spatial logarithmic strains can be computed.

If either $\tilde{H}_{iJ}$ or $\tilde{P}_{iJ}$ are given as data for the control nodes in actual computations, the macros-scale quantities are evaluated in the same way as outlined above. It is, however, noted that both the displacement $q_i^{[J]}$ and the resultant force $\tilde{R}_i^{[J]}$ cannot be specified to the same component number due to the nature of the extended system. Also, the localization procedure can be performed in exactly the same manner by using the time-series data of the macro-scale displacement gradient, which are supposed to be obtained in a macro-scale analysis.

4 Parameter identification for anisotropic hyperelastic constitutive law

After the 'measurements' with the numerical material testing, the material parameters in the assumed macroscopic constitutive model can be identified. In this section, taking a class of anisotropic hyperelastic constitutive models as an example, we introduce a method of parameter identification with all the tensor components 'measured' in the NMTs.

4.1 Strategy for parameter identification

There are some established methods of parameter identification for most isotropic hyperelasticity models available in general-purpose FEM-software. After the selection of a constitutive model that is expected to properly characterize the mechanical behavior of the rubber-like or polymeric materials under consideration, it is a common practice to perform uniaxial tension, pure shear and equi-biaxial tension tests on sheet materials [35,36]. Then, by using the measured data as input, a linear or nonlinear least square method is applied to identify the parameters used in the selected model. Although such multiple patterns of loading are prepared, it is difficult to correctly measure all the necessary components of the stress and deformation. For instance, when the membrane specimen is subjected to the uniaxial or equi-biaxial tensile loading, its out-of-plane deformation is generally not measured. Therefore, incompressibility is usually assumed in the established method of identification so that the deformation in a certain direction, which has not been measured, can be estimated from the measured data of deformation in other directions.

However, it cannot be expected that the same strategy can be applied to anisotropic hyperelastic models. In fact, deformation that is not measured cannot be reasonably estimated in anisotropic models, as a general rule. Also, since there are significantly more parameters for anisotropic models than for many isotropic models, it is necessary for the measured data to be more reliable and contain more information about the tensor components of the stress and strain than in the case of isotropic materials. In this regard, it is fortunate that we can utilize the 'empirical' data obtained from the NMT on a single *numerical specimen*, which is actually an FE model of a unit cell. That is, since the NMT enables us to evaluate all the components of the stress and strain along the deformation history of the numerical specimen, a bare minimum of data can be obtained for parameter identification of anisotropic hyperelastic constitutive functions. Of course, multiple patterns of loading are to be applied to the numerical specimen to acquire sufficient data, but the concrete patterns and their number have not yet been discussed. Thus, the present study is likely to be the first trials on the determination of the loading patterns in the NMT for parameter identification.

4.2 Loading patterns in NMT

A constitutive model is a functional representation of material behavior and essentially provides the relationship between the stress and strain tensors. That is, a constitutive model is a tensor-valued tensor function and is regarded as a device to output all the components of the stress tensor by inputting all the components of the strain tensor. In this context, we remember that the NMTs for homogenization in 3D linear elasticity are conducted on the numerical specimen, namely the unit cell model, with six-independent patterns of the macro-scale strain which have six corresponding sets of macroscopic stiffness, which is equivalent to the macroscopic stress. That is, *twenty-one* components of the macroscopic elastic coefficient matrix can be determined with only *six* NMTs. To be more specific, we apply the six-patterns of macroscopic unit strains $\mathbf{1}^{(1)} = \{1, 0, 0, 0, 0, 0\}^{\mathrm{T}} \sim \mathbf{1}^{(6)} = \{0, 0, 0, 0, 0, 1\}^{\mathrm{T}}$ to the unit cell separately, obtain the micro-scale stress $\boldsymbol{\sigma}$ and strain $\boldsymbol{\varepsilon}$, which satisfies the micro-scale BVP, and take their volume average over the unit cell to evaluate the following anisotropic elasticity matrix $\boldsymbol{D}^{\mathrm{H}}$ in the macroscopic constitutive equation $\langle\boldsymbol{\sigma}\rangle = \boldsymbol{\Sigma} = \boldsymbol{D}^{\mathrm{H}}\boldsymbol{E} = \boldsymbol{D}^{\mathrm{H}}\langle\boldsymbol{\varepsilon}\rangle$ within the linear elasticity framework:

$$\boldsymbol{D}^{\mathrm{H}} = \left[\boldsymbol{D}^{\mathrm{H}}_{(1)}\ \boldsymbol{D}^{\mathrm{H}}_{(2)}\ \boldsymbol{D}^{\mathrm{H}}_{(3)}\ \boldsymbol{D}^{\mathrm{H}}_{(4)}\ \boldsymbol{D}^{\mathrm{H}}_{(5)}\boldsymbol{D}^{\mathrm{H}}_{(6)}\right] \tag{22}$$

where each column vector $\boldsymbol{D}^{\mathrm{H}}_{(i)}$ contains the macroscopic stress components in response to i-th 'test case' with input data $\mathbf{1}^{(i)}$.

Although the macroscopic stress responses are different depending on the macroscopic strain levels for nonlinear problems, the macroscopic stress–strain curves are uniquely determined in hyperelasticity once the macroscopic deformation patterns are given. It is therefore reasonable that six-independent patterns of macroscopic deformation are given to the numerical specimen separately to obtain the six sets of response curves of six (or nine) components of the macroscopic displacement gradient tensor and 1st PK stress tensor. Using these 6×6 stress–strain curves, we are able to formulate the minimization problem to determine the unknown material parameters of an assumed constitutive function for anisotropic hyperelasticity, as detailed in the next subsection.

An example of macroscopic deformation and stress patterns in NMTs is provided in Table 1. Here, $\hat{H}$ and ■ are the specified and unspecified components of the macro-scale displacement gradient $\tilde{\boldsymbol{H}}^{[\alpha]}$ $(\alpha = 1, \cdots, 6)$, respectively, and 0 implies the value of the component is fixed to zero during the NMT. Thus, the components of the macroscopic 1st PK stress that corresponds to ■ in $\tilde{\boldsymbol{H}}^{[\alpha]}$ are zero. Also, □ and ♢ are the components of the macroscopic stress caused by the specification of $\hat{H}$ and zero in $\tilde{\boldsymbol{H}}^{[\alpha]}$, respectively. Although we admit of arbitrariness in selecting loading patterns, the material parameters are uniquely identified by the method proposed below.

4.3 Tensor-based method for parameter identification

On the presumption that the six sets of six response curves of all the components of the macroscopic displacement gradient tensor and 1st PK stress tensor have been obtained by the

Table 1 Loading patterns for numerical material tests

Case-1: Tension in the X_1-direction	Case-2: Tension in the X_2-direction
$\tilde{\boldsymbol{H}}^{[1]} = \begin{bmatrix} \hat{H} & 0 & 0 \\ 0 & \blacksquare & 0 \\ 0 & 0 & \blacksquare \end{bmatrix}, \tilde{\boldsymbol{P}}^{[1]} = \begin{bmatrix} \square & \Diamond & \Diamond \\ \Diamond & 0 & \Diamond \\ \Diamond & \Diamond & 0 \end{bmatrix}$	$\tilde{\boldsymbol{H}}^{[2]} = \begin{bmatrix} \blacksquare & 0 & 0 \\ 0 & \hat{H} & 0 \\ 0 & 0 & \blacksquare \end{bmatrix}, \tilde{\boldsymbol{P}}^{[2]} = \begin{bmatrix} 0 & \Diamond & \Diamond \\ \Diamond & \square & \Diamond \\ \Diamond & \Diamond & 0 \end{bmatrix}$
Case-3: Tension in the X_3-direction	Case-4: Shear in the X_1X_2, X_2X_1-plane
$\tilde{\boldsymbol{H}}^{[3]} = \begin{bmatrix} \blacksquare & 0 & 0 \\ 0 & \blacksquare & 0 \\ 0 & 0 & \hat{H} \end{bmatrix}, \tilde{\boldsymbol{P}}^{[3]} = \begin{bmatrix} 0 & \Diamond & \Diamond \\ \Diamond & 0 & \Diamond \\ \Diamond & \Diamond & \square \end{bmatrix}$	$\tilde{\boldsymbol{H}}^{[4]} = \begin{bmatrix} 0 & \hat{H} & 0 \\ \hat{H} & 0 & 0 \\ 0 & 0 & 0 \end{bmatrix}, \tilde{\boldsymbol{P}}^{[4]} = \begin{bmatrix} \Diamond & \square & \Diamond \\ \square & \Diamond & \Diamond \\ \Diamond & \Diamond & \Diamond \end{bmatrix}$
Case-5: Shear in the X_2X_3, X_3X_2-plane	Case-6: Shear in the X_3X_1, X_1X_3-plane
$\tilde{\boldsymbol{H}}^{[5]} = \begin{bmatrix} 0 & 0 & 0 \\ 0 & 0 & \hat{H} \\ 0 & \hat{H} & 0 \end{bmatrix}, \tilde{\boldsymbol{P}}^{[5]} = \begin{bmatrix} \Diamond & \Diamond & \Diamond \\ \Diamond & \Diamond & \square \\ \Diamond & \square & \Diamond \end{bmatrix}$	$\tilde{\boldsymbol{H}}^{[6]} = \begin{bmatrix} 0 & 0 & \hat{H} \\ 0 & 0 & 0 \\ \hat{H} & 0 & 0 \end{bmatrix}, \tilde{\boldsymbol{P}}^{[6]} = \begin{bmatrix} \Diamond & \Diamond & \square \\ \Diamond & \Diamond & \Diamond \\ \square & \Diamond & \Diamond \end{bmatrix}$

six sets of the NMTs, we introduce a method of parameter identification for anisotropic hyperelastic constitutive models. Although the method can be applied for arbitrary forms of anisotropic constitutive models, we confine ourselves to a certain class among them, in which the functional form is linear with respect to material parameters. A typical example of this class of models is presented in Appendix B, and we employ it in the following sections.

Denoting the material parameters by $p^{[k]}$ and the number of them by n_{para}, an anisotropic hyperelastic constitutive model which is linear with respect to $p^{[k]}$ can be written as

$$\tilde{\boldsymbol{S}}(\boldsymbol{p}) = \sum_{k}^{n_{\text{para}}} p^{[k]} \boldsymbol{g}^{[k]} \tag{23}$$

where $\boldsymbol{p} = \left\{p^{[1]}, \cdots, p^{[n_{\text{para}}]}\right\}$, $\tilde{\boldsymbol{S}}$ is the macroscopic 2nd Piola–Kirchhoff (PK) stress tensor and $\boldsymbol{g}^{[k]}$ ($k = 1, \cdots, \text{para}$) are tensor-valued functions that are nonlinear functions of the macroscopic deformation gradient or the alternatives. Then now, the number of deformation patterns of the NMTs is fixed to $n_{\text{test}} = 6$, and the number of 'measured' data points obtained by a NMT for loading pattern α is denoted by $n_{\text{step}}^{[\alpha]}$. More concretely, we perform micro-scale analyses $n_{\text{test}} = 6$ times for a single unit cell of the hyperelastic composite material and, for a loading pattern α, store $n_{\text{step}}^{[\alpha]}$ sets of data, each of which contains the six components of the macroscopic right Cauchy-Green (CG) deformation tnsor $\hat{\hat{\boldsymbol{C}}}^{[n,\alpha]}$C and the six components of the macroscopic 2nd PK stress tensor $\hat{\hat{\boldsymbol{S}}}^{[n,\alpha]}$ for each selected step n among the loading steps. Here, $\hat{\hat{\boldsymbol{C}}}^{[n,\alpha]}$ and $\hat{\hat{\boldsymbol{S}}}^{[n,\alpha]}$ can respectively be computed by the macroscopic displacement gradient $\hat{\hat{\boldsymbol{H}}}^{[n,\alpha]}$ and the 1st PK stress tensor $\hat{\hat{\boldsymbol{P}}}^{[n,\alpha]}$, both of them are either the input data or the 'measured' data in the NMTs as explained in the previous subsection.

On the other hand, given the data of the macroscopic displacement gradient $\hat{\hat{\boldsymbol{H}}}^{[n,\alpha]}$, the constitutive equation (23) can be evaluated to compute the corresponding macroscopic stress. We denote this constitutive response by

$$\tilde{S}_{IJ}^{[n,\alpha]}(\boldsymbol{p}) = \sum_{k}^{n_{\text{para}}} p^{[k]} g_{IJ}^{[k,n,\alpha]} \tag{24}$$

where $g_{IJ}^{[k,n,\alpha]}$ are supposed to be computed by $\hat{\hat{\boldsymbol{H}}}^{[n,\alpha]}$, or equivalently, $\hat{\hat{\boldsymbol{C}}}^{[n,\alpha]}$. Then, the following scalar-valued function can be defined to sum up the errors measured by the norms of the stress tensors:

$$\chi(\boldsymbol{p}) = \frac{1}{2} \sum_{\alpha=1}^{n_{\text{test}}} \frac{1}{n_{\text{step}}^{[\alpha]}} \left(\sum_{n=1}^{n_{\text{step}}^{[\alpha]}} \frac{\left\| \tilde{\boldsymbol{S}}^{[n,\alpha]}(\boldsymbol{p}) - \hat{\hat{\boldsymbol{S}}}^{[n,\alpha]} \right\|^2}{\left\| \hat{\hat{\boldsymbol{S}}}^{[n,\alpha]} \right\|^2} \right) \tag{25}$$

or equivalently,

$$\chi(\boldsymbol{p}) = \frac{1}{2} \sum_{\alpha=1}^{n_{\text{test}}} \frac{1}{n_{\text{step}}^{[\alpha]}} \left(\sum_{n=1}^{n_{\text{step}}^{[\alpha]}} \frac{\left(\tilde{S}_{IJ}^{[n,\alpha]}(\boldsymbol{p}) - \hat{\hat{S}}_{IJ}^{[n,\alpha]}\right)\left(\tilde{S}_{IJ}^{[n,\alpha]}(\boldsymbol{p}) - \hat{\hat{S}}_{IJ}^{[n,\alpha]}\right)}{\hat{\hat{S}}_{KL}^{[n,\alpha]} \hat{\hat{S}}_{KL}^{[n,\alpha]}} \right) \tag{26}$$

in which the summation convention is employed for the indices on the macroscopic 2nd PK stress tensor. It is to be noted that, in this error function, all the stress components are used to define the error between the constitutive response and the stress response in the NMT for the same macroscopic deformation. Note also that the role of the denominator in the error function is to normalize the error in each step n by the norm of the stress tensor obtained at the same step of the NMT and in turn to mitigate the loss of significant digits in the numerical treatments of the parameter identification.

Since the assumed constitutive equation (24) is linear with respect to the material parameters $\boldsymbol{p}$, the differentiation of the error function (25) with respect to these parameters yields the following system of linear equations to be solved for $\boldsymbol{p}$:

$$\frac{\partial \chi(\boldsymbol{p})}{\partial p^{[l]}} = 0 \quad (l = 1, \cdots, n_{\text{para}}) \tag{27}$$

To be more specific, the obtained algebraic equations are as follows:

$$\sum_{\alpha=1}^{n_{\text{test}}} \frac{1}{n_{\text{step}}^{[\alpha]}} \left\{ \left[\sum_{k=1}^{n_{\text{para}}} \sum_{n=1}^{n_{\text{step}[\alpha]}} \left(\frac{g_{IJ}^{[l,n,\alpha]} g_{IJ}^{[k,n,\alpha]}}{\hat{\tilde{S}}_{KL}^{[n,\alpha]} \hat{\tilde{S}}_{KL}^{[n,\alpha]}} \right) \right] p^{[k]} \right\}$$
$$= \sum_{\alpha=1}^{n_{\text{test}}} \frac{1}{n_{\text{step}}^{[\alpha]}} \left\{ \sum_{n=1}^{n_{\text{step}}^{[\alpha]}} \left(\frac{g_{IJ}^{[l,n,\alpha]} \hat{\tilde{S}}_{IJ}^{[n,\alpha]}}{\hat{\tilde{S}}_{KL}^{[n,\alpha]} \hat{\tilde{S}}_{KL}^{[n,\alpha]}} \right) \right\} \tag{28}$$

which can be identified with $\boldsymbol{G}\boldsymbol{p} = \boldsymbol{b}$ and solved for $\boldsymbol{p}$, if the coefficient matrix $\boldsymbol{G}$ is invertible. In fact, unless the assumed constitutive equation has some inadequacies, the regularity of the matrix should be guaranteed since the selected loading patterns provide mutually independent stress responses.

In summary the entire procedure of the proposed method is presented in the following box.

I. Select a macroscopic constitutive material model

II. Conduct NMTs on a unit cell model using FE mesh

(i) Give the macroscopic displacement gradient $\tilde{\boldsymbol{H}}$ and then the relative displacement vector $\boldsymbol{q}^{[J]}$ of the external points

$\boldsymbol{q}^{[J]} := \tilde{\boldsymbol{H}} \cdot \boldsymbol{L}^{[J]}$

(ii) Build the extended microscopic BVP Eqs. (13), (14) by imposing

$\boldsymbol{w}^{[J]} - \boldsymbol{w}^{[-J]} = \boldsymbol{q}^{[J]}$

(iii) Obtain 1st PK stress $\tilde{P}_{iJ}$ at each incremental step n for all loading patterns α from the reaction force vector directly obtained by solving the extended micro-scale BVP

$\hat{\tilde{P}}_{iJ} = \hat{\tilde{R}}_i^{[J]} / |\partial \mathcal{Y}_0^{[J]}|$

III. Identify macroscopic material parameters

(i) Using the NMT data calculate the macro-scale 2nd PK stress $\hat{\tilde{\boldsymbol{S}}}^{[n,\alpha]} \left(= \left(\tilde{\boldsymbol{F}}^{[n,\alpha]} \right)^{-1} \hat{\tilde{\boldsymbol{P}}}^{[n,\alpha]} \right)$ and the right-CG deformation tensors $\hat{\tilde{\boldsymbol{C}}}^{[n,\alpha]}$ by making use of Eq. (43) and store all sets of data over $n_{\text{step}}^{[\alpha]}$

(ii) Build a function of Eq. (23) with the material parameters $\boldsymbol{p}$

(iii) Identify the macroscopic material parameters $\boldsymbol{p}$ by solving the obtained algebraic equations $\boldsymbol{G}\boldsymbol{p} = \boldsymbol{b}$

IV. Macroscopic FE-analysis

(i) Solve the macro-scale BVP using the assumed constitutive model with identified material parameters

5 Numerical examples

Numerical analyses are conducted to demonstrate the feasibility of the two-scale coupling analysis with the micro-macro decoupling scheme and to assess the validity of the present method of parameter identification by means of the NMT. The anisotropic hyperelastic constitutive model [38,39] given in Appendix B is employed as a macro-scale material model for the macro-scale BVP, and a general-purpose FEM software, ANSYS® [37], is used for both micro- and macro-scale analyses.

5.1 Conditions for NMTs

The unit cell models for the numerical verification are shown in Figs. 3 and 4, which are referred to as UC-1 and UC-2, respectively. UC-1 is a periodic microstructure of a uni-directional fiber-reinforced composite (UD-FRC) with $\boldsymbol{A} = \{0,\ 0,\ 1\}^{\mathrm{T}}$, and UC-2 is that of a 30°-crossed fiber-reinforced composite (30CR-FRC) with $\boldsymbol{A} = \{1/2,\ 0,\ \sqrt{3}/2\}^{\mathrm{T}}$ and $\boldsymbol{B} = \{-1/2,\ 0,\ \sqrt{3}/2\}^{\mathrm{T}}$. The volume fractions of UC-1 and UC-2 are 28.3 % and 36.1 %, respectively. Also, ten-node tetrahedral elements (`SOLID 187`) in the ANSYS's element library is used for their FE meshes. For the matrix material in both of the unit cells, an isotropic hyperelastic model of Ogden [36] is assumed, and its material parameters are set at $\mu_1 = 1.9384$, $\mu_2 = 0.014$ [MPa], $\alpha_1 = 1.30$, $\alpha_2 = 5.00$

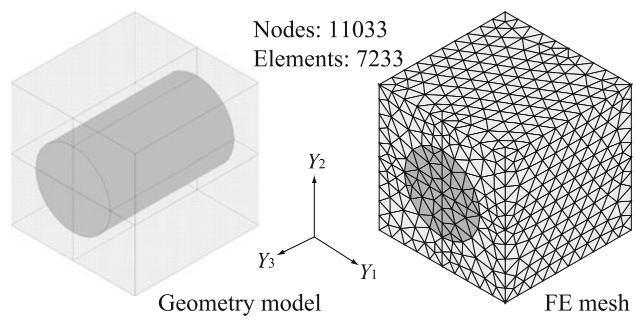

Fig. 3 UC-1: uni-directional fiber-reinforced composite.

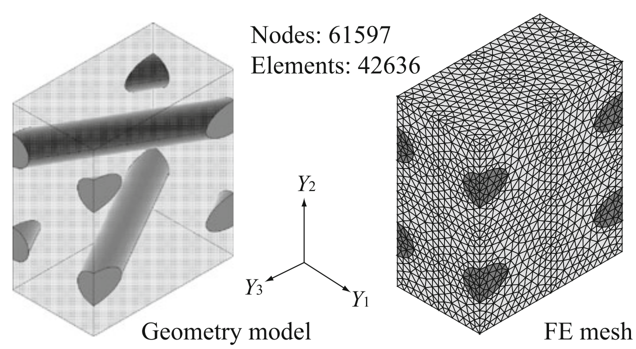

Fig. 4 UC-2: 30°-crossed fiber-reinforced composite.

and $d_{\mathrm{O}} = 1.429 \times 10^{-3}$ in the Ogden's energy functional

$$W_{\mathrm{O}} = \sum_{i=1}^{2} \frac{\mu_i}{\alpha_i} \left(\bar{\lambda}_1^{\alpha_i} + \bar{\lambda}_2^{\alpha_i} + \bar{\lambda}_3^{\alpha_i} \right) + \frac{1}{d_{\mathrm{O}}} (J-1)^2 \tag{29}$$

For the fibers, we take material parameters $\mu = 700$ [MPa] and $d_{\mathrm{H}} = 10^{-3}$ [MPa] in the following isotropic neo-Hookean energy functional:

$$W_{\mathrm{H}} = \frac{\mu}{2} \left(\bar{I}_1 - 1 \right) + \frac{1}{d_{\mathrm{H}}} (J-1)^2 \tag{30}$$

Remark 1 We have been aware that a sufficient number of digits after the decimal point is essential in recoding "measured" data in the NMTs. To be more specific, 15 or 16 digits after the decimal point are necessary to mitigate the effect of rounding errors, when we use double precision real numbers for computations. The number of digits seems to be somewhat excessive from the viewpoint of effective digits for engineering judgment, but is required for the present tensor-based method of parameter identification.

Remark 2 Similarly to Remark 1, the quality of FE meshes for unit cells is also influential on the accuracy of the NMTs and in turn that of the parameter identification demonstrated in Subsect. 5.2. For instance, we need the maximum degree of conformity in the coordinates of the nodes on the opposed sides of a unit cell, at which the two-point or three-point constraints (15) is imposed. In addition, the maximum degree of geometrical symmetry of the FE model of a unit cell is desired to obtain the symmetric motion of a geometrically symmetric unit cell in response to a macroscopically symmetric loading as in Table 1. Otherwise, the parameter identification with the present method suffers from the superfluous reaction forces at the *control nodes*.

Remark 3 The reliability of the data 'measured' in the NMT depends on the accuracy of the micro-scale analysis for the unit cell models. It is, therefore, preferable that the most fundamental response, such as a stress–strain curve of the uni-axial tension test, is calibrated so that we can eliminate any analysis errors due to the deficiencies in both the FE approximation and the input data for the unit cell models. That is, some sort of empirical validation is indispensable if the accuracy of the NMTs is essential. Nonetheless, the method of parameter identification can be verified on the assumption that the results of the NMTs are reliable enough.

5.2 NMTs and parameter identification

In Step (ii) as explained in Sect. 2.1, we conduct a series of NMTs on the two unit cell models separately by applying the six macroscopic loading patterns described in Subsect. 4.2 by means of the control points introduced in Subsect. 3.2. The number of loading steps $n_{\mathrm{step}} = 20$ is taken for each loading pattern, and the same number of sets of the macro-scale 2nd PK stress and right-CG deformation tensors, $\tilde{\boldsymbol{S}}^{[n,\alpha]}$ and $\tilde{\boldsymbol{C}}^{[n,\alpha]}$, are obtained in a single NMT with loading pattern α, as explained in Subsect. 4.3. We denote the components of the macro-scale 2nd PK stress and right-CG deformation tensors by $\hat{\tilde{C}}_{IJ}^{[n,\alpha]}$ and $\hat{\tilde{S}}_{IJ}^{[n,\alpha]}$, respectively, to distinguish them from the values determined by the assumed constitutive equation.

The results of the NMTs are shown in Figs. 5 and 6, in which only one curve is depicted for each loading pattern, although all the tensor components were obtained and stored into a file. The curves characterize the anisotropic material responses as expected. In this study, we assume the following functional form of the 2nd PK to fit these curves [38,39]:

$$\tilde{\boldsymbol{S}} = \tilde{\boldsymbol{S}}_{\mathrm{vol}} + \tilde{\boldsymbol{S}}_{\mathrm{iso}} \tag{31}$$

where

$$\tilde{\boldsymbol{S}}_{\mathrm{vol}} = \frac{2}{D} J (J-1) \tilde{\boldsymbol{C}}^{-1} \tag{32}$$

$$\begin{aligned} \tilde{\boldsymbol{S}}_{\mathrm{iso}} = I_3^{-1/3} \left(\boldsymbol{I} - \frac{1}{3} \tilde{\boldsymbol{C}}^{-1} \otimes \tilde{\boldsymbol{C}} \right) : \Big[& \bar{\gamma}_1 \boldsymbol{1} + \bar{\gamma}_2 \bar{\tilde{\boldsymbol{C}}} + \bar{\gamma}_4 (\boldsymbol{A} \otimes \boldsymbol{A}) \\ & + \bar{\gamma}_5 \left(\boldsymbol{A} \otimes \bar{\tilde{\boldsymbol{C}}} \boldsymbol{A} + \bar{\tilde{\boldsymbol{C}}} \boldsymbol{A} \otimes \boldsymbol{A} \right) + \bar{\gamma}_6 (\boldsymbol{B} \otimes \boldsymbol{B}) \\ & + \bar{\gamma}_7 \left(\boldsymbol{B} \otimes \bar{\tilde{\boldsymbol{C}}} \boldsymbol{B} + \bar{\tilde{\boldsymbol{C}}} \boldsymbol{B} \otimes \boldsymbol{B} \right) + \bar{\gamma}_8 (\boldsymbol{A} \otimes \boldsymbol{B}) \Big] \end{aligned} \tag{33}$$

Here, $\bar{\gamma}_i$ $(i = 1, \cdots, 8)$ and D are described in Appendix B. This expression of the stress corresponds to UC-2, whereas UC-1 should provide the transversely isotropic behavior that can be realized by setting $\boldsymbol{B} = \boldsymbol{0}$ in (33); see [38].

Now, let us go on to the Step (iii) as described in Sect. 2.1. That is, we apply the method of parameter identification, which is proposed in Subsect. 4.3, to identify the material parameters of the assumed constitutive equation. To be more specific, the material parameters to be determined are $a_i,\ b_i,\ c_i$ $(i = 1, 2, 3)$ and $d_i,\ e_i,\ f_i,\ g_i$ $(i = 2, \cdots, 6)$ in (51) as well as D in (32) or (50), though the parameters $e_i,\ f_i,\ g_i$ are unnecessary for UC-1 as mentioned before. The value of the error function (25) for each loading pattern is presented in Table 2. Using the identified parameters in (24) for the assumed constitutive model and the same $\hat{\tilde{C}}_{IJ}^{[n,\alpha]}$ used in the NMTs for the arguments $\tilde{C}_{IJ}^{[n,\alpha]}$, we provide the functional responses of $\tilde{S}_{IJ}^{[n,\alpha]}$ in Figs. 7, 9 and 8, where the results of the NMTs are also shown for comparison. The macro-scale stress–strain curves in Figs. 7 and 8 are the responses to the macro-scale deformation patterns consistent with the NMTs, while those in Fig. 9 are not realized in the NMTs. In particular, Fig. 9a shows the macroscopic response of UC-1 when tensile loading is applied in the Y_1-direction with the Y_2-direction stress free and with the Y_3-direction fixed, and Fig. 9b shows the relationships between the macroscopic axial stress components and the right CG deformation tensor components of UC-2 when tensile loading is applied in each

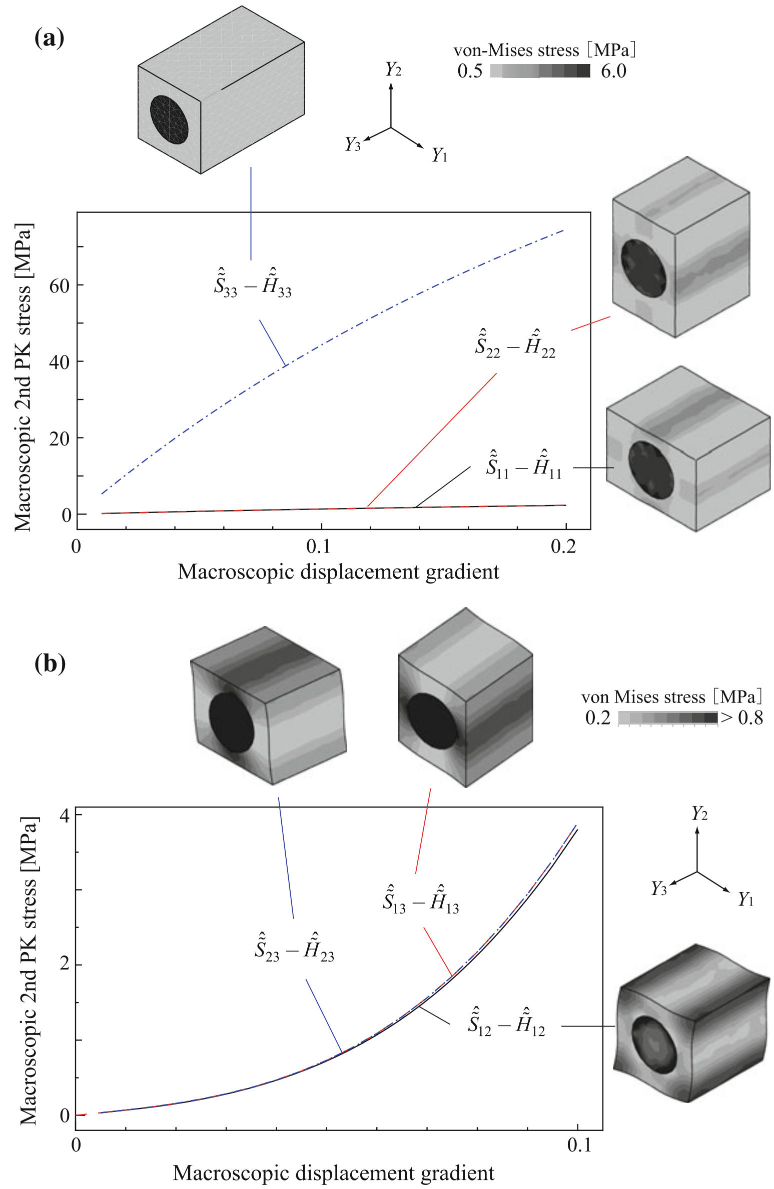

Fig. 5 Numerical material test results for unit cell of uni-directional fiber-reinforced composite: **a** three normal normal components; **b** three shear components.

one of the normal directions with the side lengths in the other two directions fixed.

It can be seen from Figs. 7a, b for UC-1 that the curves obtained with the identified parameters show fairly good agreement with those of the NMTs, although conformity may not be satisfactory, especially in the case of the shear deformation patterns. These levels of accuracy are also seen in Table 2. As can be seen from Fig. 9a, some level of accuracy is observed in response to the loading patterns not contained in the six patterns in the NMTs for parameter identifcation. A note is appended with regard having obtained equivalent results for other kinds of unit cells of UD-FRC of different volume fractions of fibers.

Similar studies can be made on the results shown in Fig. 8 for UC-2, which compares the constitutive responses with the identified parameters and the data obtained in NMTs for the macroscopically orthotropic behavior of the 30CR-FRC. Although the disagreement in the response $\hat{\tilde{C}}_{33}^{[n,\alpha]} \sim \hat{\tilde{S}}_{33}^{[n,\alpha]}$ is by no means small and is confirmable in Table 2, the parameter identification seems to be largely successful. The reason why the error calculated for the 2nd pattern with $\tilde{H}_{22}$ being controlled in the NMT is relatively large in Table 2, even though fairly good agreement is obtained for the response in $\tilde{S}_{22} \sim \tilde{C}_{22}$, is that the functional responses of some components other than $\tilde{S}_{22} \sim \tilde{C}_{22}$ to this loading pattern deviate from those of the NMTs. We tried other error functions besides (25), but failed to obtain better results.

The assumed constitutive model for orthotropic hyperelasticity is not capable of accurately reproducing the material behavior expected from the prepared unit cell models,

Fig. 6 Numerical material test results unit cell of 30°-crossed fiber-reinforced composite: **a** three normal normal components; **b** three shear components.

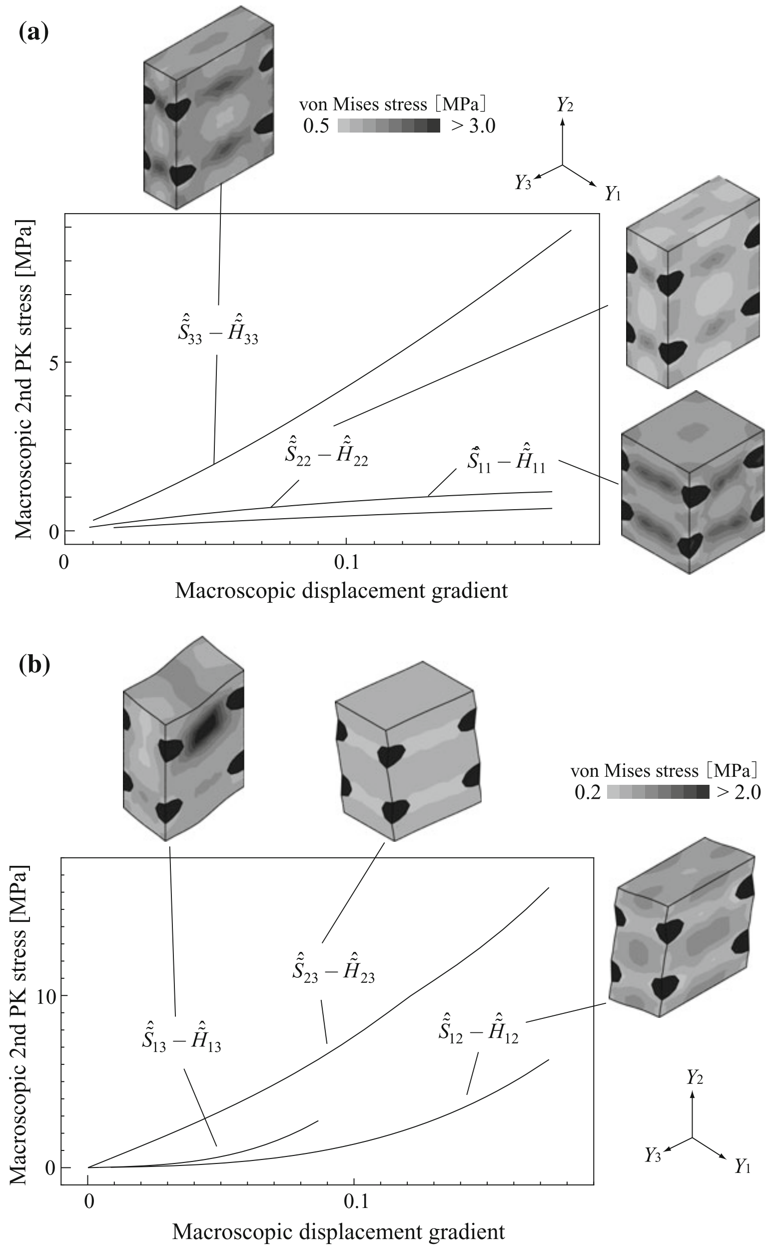

Table 2 Square errors in parameter identification

Loading patterns in NMT	1	2	3	4	5	6
UC-1	9.187×10^{-6}	9.187×10^{-6}	9.577×10^{-5}	0.01238	0.01033	0.01033
UC-2	0.07770	0.1949	0.05057	0.008249	0.01963	0.001126

though the level of accuracy in the parameter identification is assured to some extent. It was, however, not until the parameter identification was realized by means of the NMTs that the performance of the constitutive model was examined in this study. If there were more appropriate constitutive models available, the present approach for homogenization in the two-scale analyses could be advocated.

5.3 Parameter identification for non-proportional loading

In this numerical example, non-proportional loading condition is considered in terms of the unit cell model UC-1 to verify the further quality of the parameter identification. We use the material parameters obtained at Subsect. 5.2 and compare the analysis results with the identified

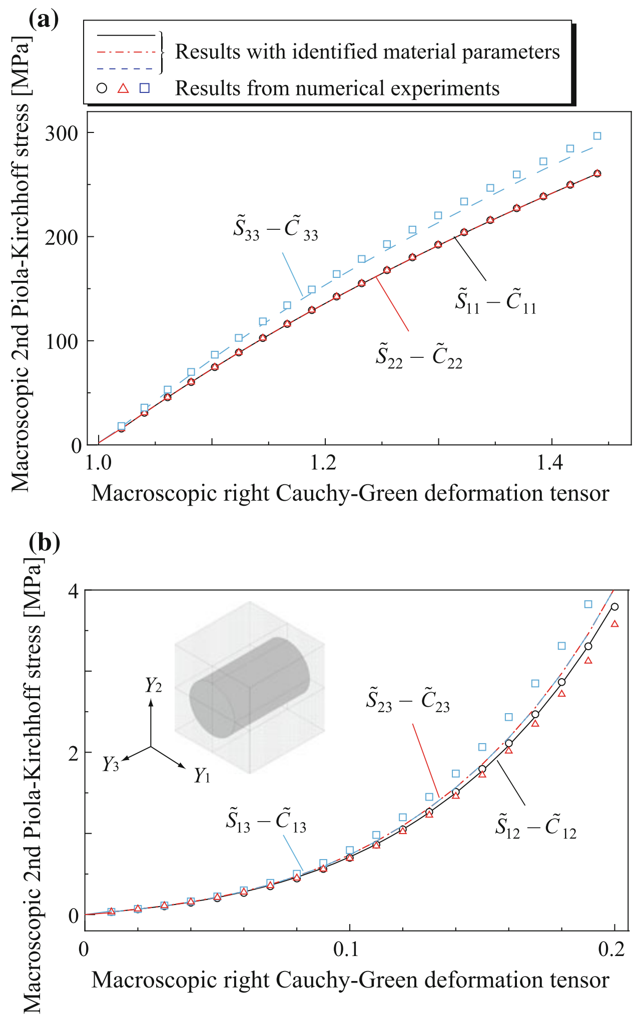

Fig. 7 Fitting results for unit cell of uni-directional fiber-reinforced composite. Fundamental responses as in NMTs: **a** three normal normal components; **b** three shear components.

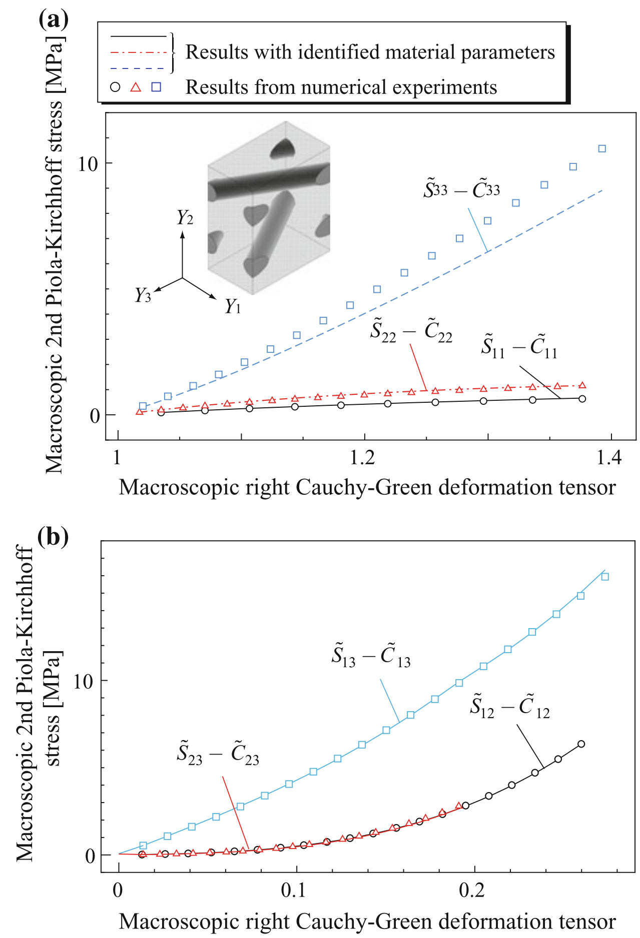

Fig. 8 Fitting results for unit cell of 30°-crossed fiber-reinforced composite: **a** three normal normal components; **b** three shear components.

material parameters and by the micro-scale analysis. The assumed non-proportional loading is uniform tension in the Y_1-direction followed by unloading and transverse shear in the Y_{12}-direction. To be more specific, the following two macroscopic displacement gradients, expressed as $\tilde{\boldsymbol{H}}^{(1)}$ and $\tilde{\boldsymbol{H}}^{(2)}$, are given to the three external material points in turn as constraints,

$$\tilde{\boldsymbol{H}}^{(1)} = \begin{bmatrix} 0.15 & 0 & 0 \\ 0 & \blacksquare & 0 \\ 0 & 0 & \blacksquare \end{bmatrix}, \quad \tilde{\boldsymbol{H}}^{(2)} = \begin{bmatrix} 0 & 0.15 & 0 \\ 0.15 & \blacksquare & 0 \\ 0 & 0 & \blacksquare \end{bmatrix} \tag{34}$$

where the superscript denotes simply the order of applied loading condition.

Figure 10 shows the results of the analysis with the identified material parameters and of the micro-scale analysis using the UC-1. Here, the relation of the equivalent 2nd PK stress and the equivalent displacement gradient is displayed to examine the response with respect to the non-proportional loading. It is observed that the response shows almost linear behavior during the deformation by $\tilde{\boldsymbol{H}}^{(1)}$, then turns out to be complex nonlinear behavior during the deformation by $\tilde{\boldsymbol{H}}^{(2)}$. As can be seen, the result with identified material parameters shows good agreement with the micro-scale analysis, although discrepancy is observed between two responses. In general, this kind of errors tend to be accumulated and increased as the loading direction is changed frequently. However, the present errors occur during the deformation by $\tilde{\boldsymbol{H}}^{(1)}$ and thereafter still preserve almost constant even under the complex response by $\tilde{\boldsymbol{H}}^{(2)}$. This means that the parameter identification was successfully implemented and the identified parameters provide sufficient quality for the macro-scale analysis within the scope of errors in Table 2.

5.4 Macro-scale and micro-scale analyses

The next step, namely Step (iv), is to conduct the macroscopic analysis with the assumed macroscopic constitutive

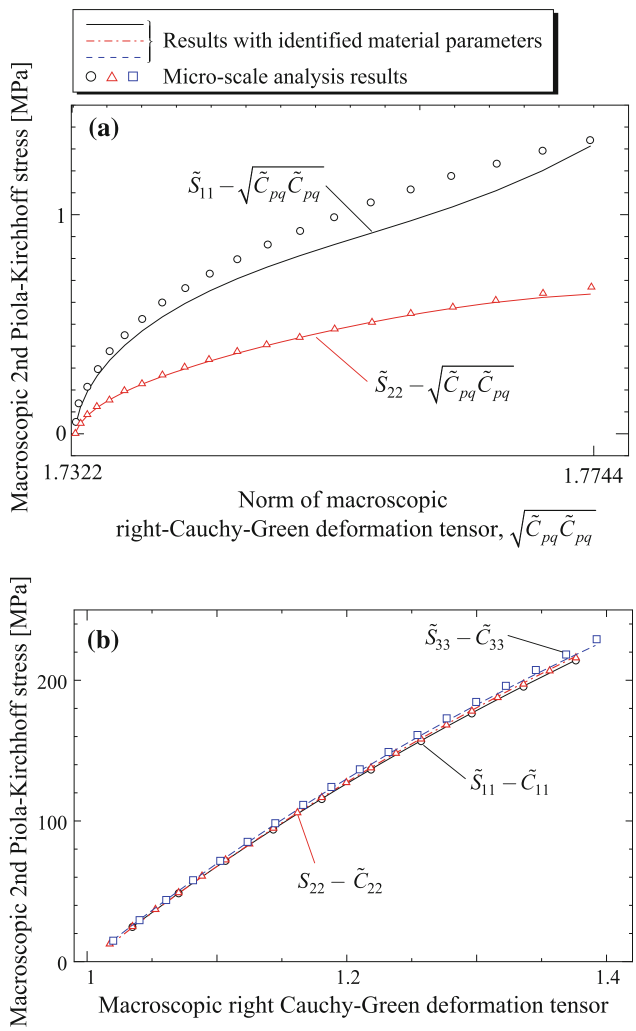

Fig. 9 Responses to the macro-scale deformation patterns not realized in NMTs: **a** macroscopic response of UC-1 when tensile loading is applied in the Y_1-direction with the Y_2-direction stress free and with the Y_3-direction fixed; **b** relationships between the macroscopic axial stress components and the right CG deformation tensor components of UC-2 when tensile loading is applied in each one of the normal axial directions with the side lengths in the other two directions fixed.

model using the material parameters identified above. Below, a demonstration is made only for the UC-1 of Fig. 3.

We consider the macro-structure as shown in Fig. 11, which also illustrates the support and loading conditions. Here, the micro-scale coordinate system O-$Y_1'Y_2'Y_3'$ is different from that used in the NMTs in Step (ii) in this example. More specifically, the fiber direction parallel to the Y_3-axis is rotated by 60° in the counterclockwise direction with respect to the X_2 axis that is identical with the Y_2 axis, while the Y_2 and Y_2'-axes are identical. Knowing that the macro-scale coordinate system in Steps (ii) and (iii) coincides with the micro-scale one, we have to set the fiber direction at $\boldsymbol{A} = \{1/2,\ 0,\ \sqrt{3}/2\}^{\mathrm{T}}$ along with $\boldsymbol{B} = \boldsymbol{0}$ for (33).

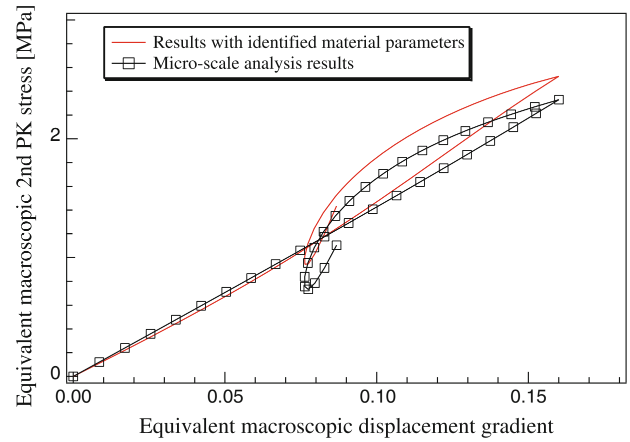

Fig. 10 Comparison of analysis result applying identified material parameters with result of macro-scale analysis.

After the macro-scale analysis, the localization analysis in Step (v) can be performed, if necessary, by using the macroscopic deformation histories obtained in the macro-scale analysis in Step (iv) at certain points of interest in the macro-structure. In this example, after selecting the center points of two representative elements, Points A and B, indicated in Fig. 11, we extract the time-series data of the macro-scale displacement gradient tensors at these points. Before applying the values to each unit cell to carry out the corresponding micro-scale analysis for localization, the tensor components of the macro-scale displacement gradients have to be transformed to the values in the rotated macro-scale coordinate system O-$X_1'X_2'X_3'$ whose axes conform with the micro-scale system O-$Y_1'Y_2'Y_3'$. That is, we need to transform the time series data of $\tilde{H}_{pq}$ at Points A and B by the following coordinate transformation rule:

$$\tilde{H}'_{ij} = \sum_{p=1}^{3}\sum_{q=1}^{3} T_{ip}\tilde{H}_{pq}T_{jq} \tag{35}$$

where T_{ij} are the components of the coordinate transformation matrix defined for this particular example as

$$[T] = \begin{bmatrix} \cos\theta & 0 & \sin\theta \\ 0 & 1 & 0 \\ -\sin\theta & 0 & \cos\theta \end{bmatrix} \tag{36}$$

with θ being set at 60°. By applying the components $\tilde{H}'_{ij}$ at Points A and B to the control nodes with reference to (15) and (16), we carry out the micro-scale analyses to evaluate the actual micro-scale stress and strain in the corresponding unit cells.

Figure 12 shows the results of both the macro-scale analysis and the localization analyses associated with Points A and B for the loading step 20/40 and 40/40. As can be seen from the figure, each micro-scale motion properly reflects

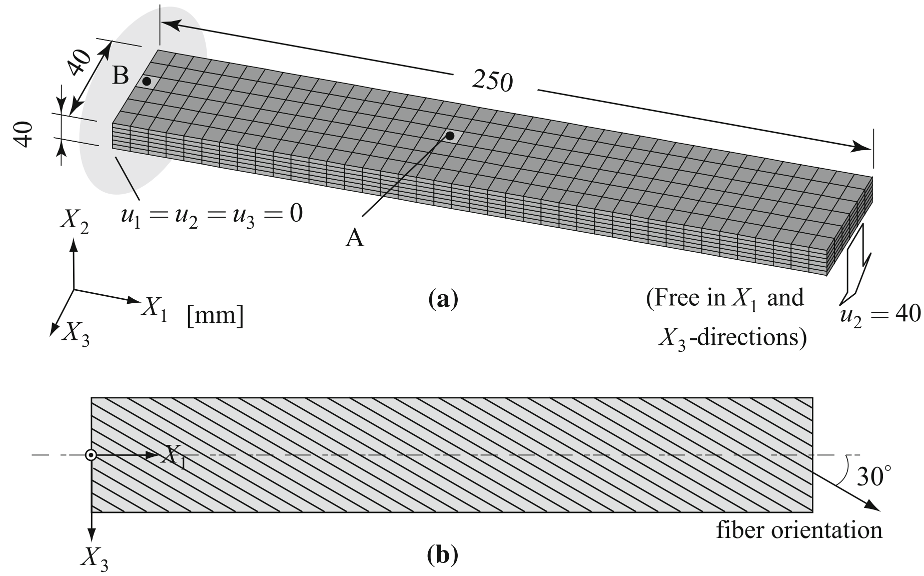

Fig. 11 Macroscopic problem: **a** FE model with boundary conditions; **b** fiber alignment.

the corresponding macro-scale displacement gradient at the selected points of interest in the macro-structure. Concretely speaking, the unit cell located at Point A is dominated by a rigid-body rotation with shear deformation mainly due to the inclined fiber, while the unit cell at Point B exhibits stretching in the X_1-direction with a relatively high stress value but without severe a-rigid-body rotation. The results carry the implication of the so-called two-scale kinematics introduced in [34], and thus illustrate that the macro-scale *material* behavior is consistent with the micro-scale *structural* response in the proposed method of two-scale analysis.

By comparing the macro-scale stresses obtained from the micro- and macro-scale analyses, we can conduct the verification of the results. In fact, the localization analysis for each selected point enables us to compute the reaction forces at the control nodes (17) and in turn the macroscopic stress with (18). It was confirmed that the macroscopic stress computed this way was almost the same as that obtained by the macro-scale analysis, though the overlapped two stress–strain curves are not shown here. Accordingly, it can be concluded that the proposed method of two-scale analysis with the micro–macro decoupling scheme is reliable enough to the extent of the adequacy of the assumed macroscopic constitutive model.

6 Concluding remarks

Intending to develop a multiscale CAE system for composite materials, we have introduced a method of two-scale analysis by applying the micro-macro decoupling scheme under the assumption that a functional form of the macroscopic constitutive equation is available. The key ingredient of the method is the numerical material testing, which corresponds to the homogenization process realized by carrying out micro-scale numerical analyses for periodic microstructures (unit cells) of composite materials. To be more specific, assuming that the concrete functional form of the macroscopic constitutive model is known, a series of numerical materials tests (NMTs) is conducted on the *numerical specimen*, i.e., the unit cell's FE model, to obtain the nonlinear macro-scale material behavior. This has been successfully conducted thanks to the introduction of the extended system for the two-scale BVP, and the corresponding micro-scale analyses have been realized by a general-purpose FEM code by virtue of the utilization of the *control nodes* located outside the unit cell model. Then, the proposed tensor-based method of parameter identification enables us to determine the material parameters in the assumed model by means of the 'measured' data in the NMTs. Once the macro-scale material behavior fitted with the identified parameters is satisfactory to us, the macro-scale analysis can be performed, which must be conducive in the macro-scale CAE. Moreover, as may be necessary, we are able to carry out the micro-scale analysis to evaluate micro-scale mechanical behavior of the unit cell associated with a macro-scale point, by applying the macro-scale deformation history at that point to the *control nodes*. This final process suggests the possibility of the micro-scale CAE. Taking an anisotropic hyperelastic constitutive model of fiber-reinforced composites as an example of the assumed macroscopic material behavior, we have demonstrated the potential and promise of the method.

A foreseeable extension of this study would be to develop a CAE system that enables us to deal with a variety of material behavior arising from arbitrary kinds of microstructures. The bottleneck in development must come in the form of a reliable macro-scale constitutive equation, which should be, ideally, represent the actual macro-scale material behavior. Therefore, the development of relevant constitutive mod-

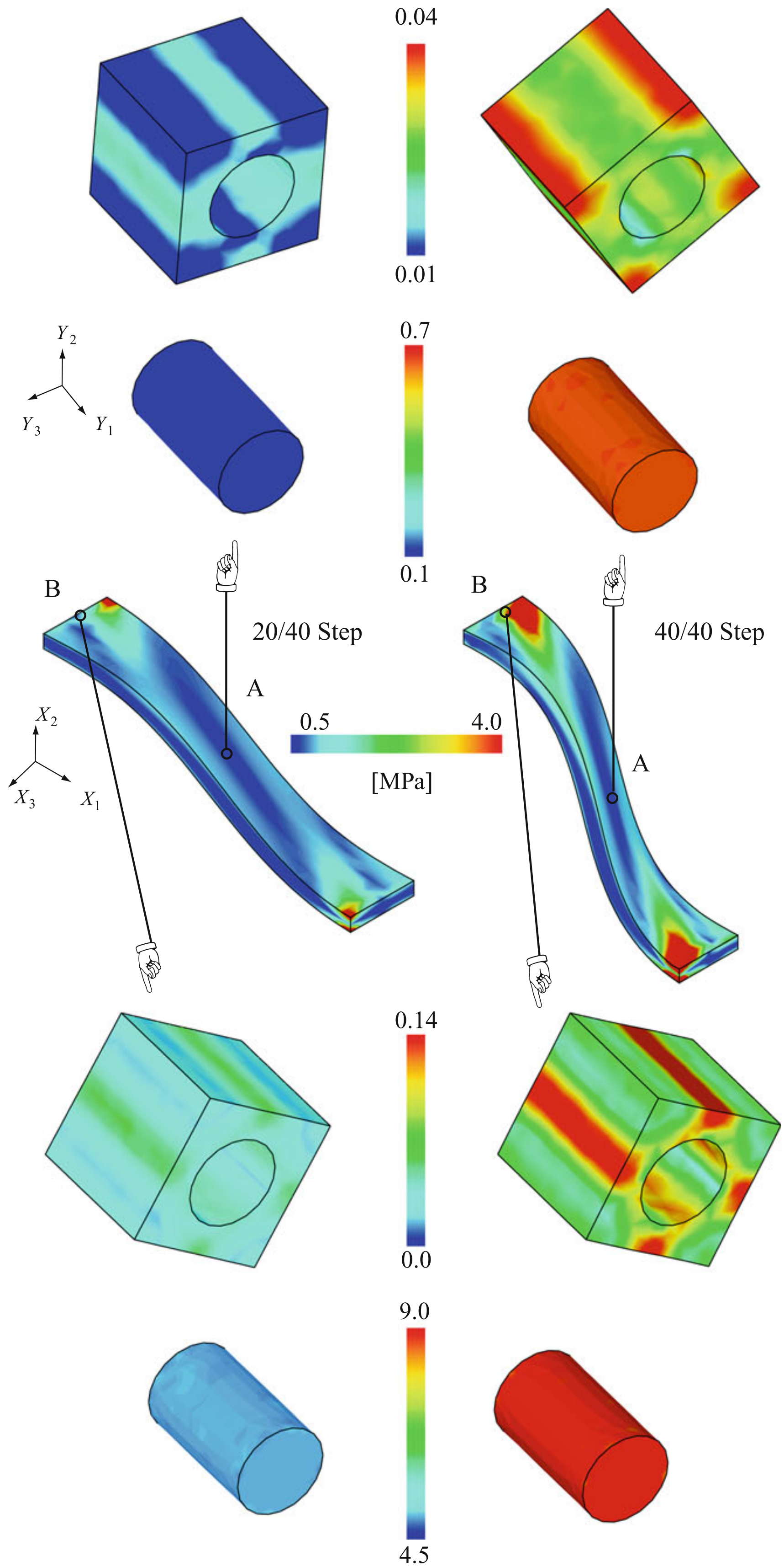

Fig. 12 Macro- and microscopic analysis results.

els and the improvement of existing models should be promoted simultaneously with the development of the system. The extensive utilization of the NMT technology is expected to make it possible.

Acknowledgments The authors would like to acknowledge the Nonlinear Homogenization Research Group consisting of Tohoku University, Nitto Boseki Co., Ltd. and Quint Corporation, in particular Dr. Keizo Ishii and Mr. Makoto Tsukino (Quint Corporation), Mr. Koji Yamamoto, Mr. Tomohiro Ishida, Mr. Akio Miyori, Mr. Fukagawa (Cybernet Systems, Co. Ltd.), and Mr. Naohiro Miyanaga (Nitto Boseki Co., Ltd.) for their contributions and discussions in developing a linear and nonlinear mutli-scale analysis code "Multiscale.Sim", which is embedded in ANSYS® software.

Relationship between the macro- and micro-scale traction vectors

In this appendix, we derive relationship (11), which is critical to the numerical material testing with a general-purpose FEM software. For the sake of simplicity, a rectangular parallelepipe-shaped unit cell is considered, with its boundary surfaces assumed to be perpendicular to one of the axes of the micro-scale coordinate system so that only the J-th component of the side vector $\boldsymbol{L}^{[J]}$ is a non-zero value L_J $(J = 1, 2, 3)$. In other words, the J-th basis vector $\boldsymbol{E}^{[J]}$ coincides with the outward unit normal vector of the side vector $\boldsymbol{L}^{[J]}$ of the unit cell of $L_1 \times L_2 \times L_3$. It is also assumed that the basis vectors $\boldsymbol{E}^{[1]}$, $\boldsymbol{E}^{[2]}$, $\boldsymbol{E}^{[3]}$ are common to the micro- and macro-scale coordinate systems, O-$Y_1Y_2Y_3$ and O-$X_1X_2X_3$.

As indicated in Eq. (6), the macroscopic 1st Piola–Kirchhoff (PK) stress $\tilde{\boldsymbol{P}}$ is the volumetric average of the corresponding microscopic stress $\boldsymbol{P}$ over the domain of the initial configuration $\mathcal{Y}_0$ of a unit cell. This homogenization formula for the stress can be transformed to

$$\begin{aligned}\tilde{\boldsymbol{P}} &= \frac{1}{|\mathcal{Y}_0|}\int\limits_{\mathcal{Y}_0}[\nabla_Y\cdot(\boldsymbol{P}\otimes\boldsymbol{Y})-(\nabla_Y\cdot\boldsymbol{P})\otimes\boldsymbol{Y}]dY\\ &= \frac{1}{|\mathcal{Y}_0|}\int\limits_{\mathcal{Y}_0}\nabla_Y\cdot(\boldsymbol{P}\otimes\boldsymbol{Y})dY \end{aligned} \tag{37}$$

where we have used the micro-scale self-equilibrium equation (3) along with $\nabla_Y \cdot (\boldsymbol{P}\otimes\boldsymbol{Y}) = (\nabla_Y\cdot\boldsymbol{P})\otimes\boldsymbol{Y} + \boldsymbol{P}$. The application of the Gauss divergence theorem yields the following relationship:

$$\tilde{\boldsymbol{P}} = \frac{1}{|\mathcal{Y}_0|}\int\limits_{\partial\mathcal{Y}_0}(\boldsymbol{P}\otimes\boldsymbol{Y})\cdot\boldsymbol{N}ds = \frac{1}{|\mathcal{Y}_0|}\int\limits_{\partial\mathcal{Y}_0}\boldsymbol{T}^{(N)}\otimes\boldsymbol{Y}ds \tag{38}$$

where $\boldsymbol{T}^{(N)} := \boldsymbol{P}\cdot\boldsymbol{N}$ is the microscopic Piola traction vector, wtth $\boldsymbol{N}$ being an arbitrary outward unit normal vector at the boundary surface $\partial\mathcal{Y}_0$. Note here that, due to the assumption on the geometry of the unit cell, the outward unit normal vector $\boldsymbol{N}$ at the unit cell boundairs $\partial\mathcal{Y}_0^{[J]}$ coincides with $\boldsymbol{E}^{[J]}$.

Since the same basis vectors are used for the micro- and macro-scale coordinate systems, the macro-scale Piola traction vector on the macroscopic surface, which is parallel to the boundary surface $\partial\mathcal{Y}_0^{[J]}$ with the outward unit normal vector $\boldsymbol{E}^{[J]}$ can be can be written as the area average of the corresponding micro-scale Piola traction vector on $\partial\mathcal{Y}_0^{[J]}$. For example, the macro-scale Piola traction vector $\tilde{\boldsymbol{T}}^{(\boldsymbol{E}^{[1]})}$ associated with $\partial\mathcal{Y}_0^{[1]}$ and $\boldsymbol{E}^{[1]}$, whose compnents are $\{1,\ 0,\ 0\}^{\mathrm{T}}$, can be expressed as follows:

$$\begin{aligned}\tilde{\boldsymbol{T}}^{(\boldsymbol{E}^{[1]})} &= \tilde{\boldsymbol{P}}\cdot\boldsymbol{E}^{[1]}\\ &= \left(\frac{1}{|\mathcal{Y}_0|}\int\limits_{\partial\mathcal{Y}_0}\boldsymbol{T}^{(N)}\otimes\boldsymbol{Y}dS\right)\cdot\boldsymbol{E}^{[1]} = \frac{1}{|\mathcal{Y}_0|}\int\limits_{\partial\mathcal{Y}_0}\boldsymbol{T}^{(N)}Y_1dS\\ &= \frac{1}{|\mathcal{Y}_0|}\left(\int\limits_{\partial\mathcal{Y}_0^{[1]}}\boldsymbol{T}^{(\boldsymbol{E}^{[1]})}Y_1dS + \int\limits_{\partial\mathcal{Y}_0^{[-1]}}\boldsymbol{T}^{(\boldsymbol{E}^{[-1]})}Y_1S\right.\\ &\quad + \int\limits_{\partial\mathcal{Y}_0^{[2]}}\boldsymbol{T}^{(\boldsymbol{E}^{[2]})}Y_1dS + \int\limits_{\partial\mathcal{Y}_0^{[-2]}}\boldsymbol{T}^{(\boldsymbol{E}^{[-2]})}Y_1dS\\ &\quad \left.+ \int\limits_{\partial\mathcal{Y}_0^{[3]}}\boldsymbol{T}^{(\boldsymbol{E}^{[3]})}Y_1dS + \int\limits_{\partial\mathcal{Y}_0^{[-3]}}\boldsymbol{T}^{(\boldsymbol{E}^{[-3]})}Y_1dS\right)\end{aligned} \tag{39}$$

where Eq. (38) has been utilized. Then, due to the anti-periodicity of the Piola traction vector (4), we apply $\boldsymbol{T}^{(\boldsymbol{E}^{[-J]})} = -\boldsymbol{T}^{(\boldsymbol{E}^{[J]})}$ along with $Y_1|_{\partial\mathcal{Y}_0^{[J]}} = Y_1|_{\partial\mathcal{Y}_0^{[-J]}}$ $(J \neq 1)$ to (39) to have

$$\tilde{\boldsymbol{T}}^{(\boldsymbol{E}^{[1]})} = \frac{Y_1|_{\partial\mathcal{Y}_0^{[1]}} - Y_1|_{\partial\mathcal{Y}_0^{[-1]}}}{|\mathcal{Y}_0|}\int\limits_{\partial\mathcal{Y}_0^{[1]}}\boldsymbol{T}^{(\boldsymbol{E}^{[1]})}dS. \tag{40}$$

Using the equivalent expressions $L_1 = Y_1|_{\partial\mathcal{Y}_0^{[1]}} - Y_1|_{\partial\mathcal{Y}_0^{[-1]}}$, $|\mathcal{Y}_0| = L_1L_2L_3$ and $\left|\partial\mathcal{Y}_0^{[1]}\right| = L_2L_3$, we arrive at the following relationship:

$$\tilde{\boldsymbol{T}}^{(\boldsymbol{E}^{[1]})} = \tilde{\boldsymbol{P}}\cdot\boldsymbol{E}^{[1]} = \frac{1}{|\partial\mathcal{Y}_0^{[1]}|}\int\limits_{\partial\mathcal{Y}_0^{[1]}}\boldsymbol{T}^{(\boldsymbol{E}^{[1]})}ds \tag{41}$$

Since the same expression can be obtained for the traction vectors on the other two boundary surfaces, Eq. (11) has been proven.

Anisotropic hyperelastic model with fabric vectors

We consider one class of anisotropic hyperelastic constitutive models, whose functional form is expressed by means of the invariants of the right Cauchy-Green (CG) deformation tensor $\boldsymbol{C}$ along with the so-called "fabric" vector indicating the direction of reinforcements such as fibers. Although the application for the macroscopic BVP is assumed, we do not distinguish the micro- and macro-scale variables below.

The elastic energy functional of the employed anisotropic hyperelastic model is given as

$$W = W_{\text{vol}}(J) + W_{\text{iso}}\left(\bar{\boldsymbol{C}}; \boldsymbol{A}, \boldsymbol{B}\right) \tag{42}$$

where $\boldsymbol{A}$ and $\boldsymbol{B}$ are the two distinct directions of fiber alignment in the reference configuration and can be referred to as the fibric vectors. Here, $W_{\text{vol}}(J)$ is the energy function of the Jacobian $J := \det \boldsymbol{F}$ associated with the volumetric deformation. $W_{\text{iso}}\left(\bar{\boldsymbol{C}}; \boldsymbol{A}, \boldsymbol{B}\right)$ is the isochoric component of the energy functional by means of the deviatoric part of the right CG deformation tensor, which is defined as

$$\bar{\boldsymbol{C}} = \bar{\boldsymbol{F}}^{\mathrm{T}}\bar{\boldsymbol{F}} = J^{-2/3}\boldsymbol{F}^{\mathrm{T}}\boldsymbol{F} = I_3^{-1/3}\boldsymbol{C} \tag{43}$$

with $\bar{\boldsymbol{F}} = J^{-1/3}\boldsymbol{F}$ and $I_3 = \det \boldsymbol{C} = J^2$.

The 2nd Piola–Kirchhoff (PK) stress can be obtained by differentiating the energy function (42) with respect to the right CG deformation tensor $\boldsymbol{C}$ as follows:

$$\boldsymbol{S} = 2\frac{\partial W}{\partial \boldsymbol{C}} = 2\frac{\partial W_{\text{vol}}}{\partial \boldsymbol{C}} + 2\frac{\partial W_{\text{iso}}}{\partial \boldsymbol{C}} = \boldsymbol{S}_{\text{vol}} + \boldsymbol{S}_{\text{iso}} \tag{44}$$

Here, we have defined the volumetric and isochoric components of $\boldsymbol{S}$, $\boldsymbol{S}_{\text{vol}}$ and $\boldsymbol{S}_{\text{iso}}$, are respectively expressed as

$$\boldsymbol{S}_{\text{vol}} = 2\frac{\partial W_{\text{vol}}}{\partial \boldsymbol{C}} = J\frac{\partial W_{\text{vol}}}{\partial J}\boldsymbol{C}^{-1} \tag{45}$$

$$\boldsymbol{S}_{\text{iso}} = I_3^{-1/3}\mathbb{Q} : \bar{\boldsymbol{S}} \tag{46}$$

where

$$\mathbb{Q} = \boldsymbol{I} - \frac{1}{3}\boldsymbol{C}^{-1} \otimes \boldsymbol{C} \tag{47}$$

$$\begin{aligned}\bar{\boldsymbol{S}} &= 2\frac{\partial W_{\text{iso}}}{\partial \bar{\boldsymbol{C}}} \\ &= \bar{\gamma}_1\mathbf{1} + \bar{\gamma}_2\bar{\boldsymbol{C}} + \bar{\gamma}_4(\boldsymbol{A}\otimes\boldsymbol{A}) + \bar{\gamma}_5\left(\boldsymbol{A}\otimes\bar{\boldsymbol{C}}\boldsymbol{A} + \bar{\boldsymbol{C}}\boldsymbol{A}\otimes\boldsymbol{A}\right) \\ &\quad + \bar{\gamma}_6(\boldsymbol{B}\otimes\boldsymbol{B}) + \bar{\gamma}_7\left(\boldsymbol{B}\otimes\bar{\boldsymbol{C}}\boldsymbol{B} + \bar{\boldsymbol{C}}\bar{\boldsymbol{B}}\otimes\boldsymbol{B}\right) \\ &\quad + \bar{\gamma}_8(\boldsymbol{A}\cdot\boldsymbol{B})(\boldsymbol{A}\otimes\boldsymbol{B})\end{aligned} \tag{48}$$

along with

$$\left.\begin{aligned}&\bar{\gamma}_1 = 2\left(\frac{\partial W_{\text{iso}}}{\partial \bar{I}_1} + \bar{I}_1\frac{\partial W_{\text{iso}}}{\partial \bar{I}_2}\right), \\ &\bar{\gamma}_2 = -2\frac{\partial W_{\text{iso}}}{\partial \bar{I}_2}, \quad \bar{\gamma}_4 = 2\frac{\partial W_{\text{iso}}}{\partial \bar{I}_4}, \quad \bar{\gamma}_5 = 2\frac{\partial W_{\text{iso}}}{\partial \bar{I}_5}, \\ &\bar{\gamma}_6 = 2\frac{\partial W_{\text{iso}}}{\partial \bar{I}_6}, \quad \bar{\gamma}_7 = 2\frac{\partial W_{\text{iso}}}{\partial \bar{I}_7}, \quad \bar{\gamma}_8 = 2\frac{\partial W_{\text{iso}}}{\partial \bar{I}_8}\end{aligned}\right\} \tag{49}$$

Here, $\mathbf{1}$ and $\boldsymbol{I}$ are the 2nd-order identity tensor and the 4th-order symmetric identify tensor, respectively. Information about the derivation of these formulae is found in [40].

One of the examples of this class is typified by Kaliske et al. [38,39], which seems to be reasonable within the present framework of two-scale coupling analysis with the micro-macro decoupling scheme. We employ their model in this study and provide its concrete functional form below. The volumetric and isochoric parts of the energy functional in [39] by are respectively given as

$$W_{\text{vol}} = \frac{1}{D}(J-1)^2 \tag{50}$$

$$\begin{aligned}W_{\text{iso}} &= W_{\text{iso}}(\bar{I}_1, \bar{I}_2, \bar{I}_4, \bar{I}_5, \bar{I}_6, \bar{I}_7, \bar{I}_8; a_i, b_j, c_k, d_l, e_m, f_n, g_o; \boldsymbol{A}, \boldsymbol{B}) \\ &= \sum_{i=1}^{3} a_i\left(\bar{I}_1 - 3\right)^i + \sum_{j=1}^{3} b_j\left(\bar{I}_2 - 3\right)^j \\ &\quad + \sum_{k=2}^{6} c_k\left(\bar{I}_4 - 1\right)^k + \sum_{l=2}^{6} d_l\left(\bar{I}_5 - 1\right)^l + \sum_{m=2}^{6} e_m\left(\bar{I}_6 - 1\right)^m \\ &\quad + \sum_{n=2}^{6} f_n\left(\bar{I}_7 - 1\right)^n + \sum_{o=2}^{6} g_o\left(\bar{I}_8 - \varsigma\right)^o\end{aligned} \tag{51}$$

Here, $D, a_i, b_j, c_k, d_l, e_m, f_n, g_o$ are scalar-valued material parameters, and $\bar{I}_1, \bar{I}_2, \bar{I}_4, \bar{I}_5, \bar{I}_6, \bar{I}_7, \bar{I}_8$ are the invariant of $\bar{\boldsymbol{C}}$ defined as follows:

$$\left.\begin{aligned}&\bar{I}_1 = \mathrm{tr}\bar{\boldsymbol{C}}, \quad \bar{I}_2 = \frac{1}{2}\left(\mathrm{tr}^2\bar{\boldsymbol{C}} - \mathrm{tr}\bar{\boldsymbol{C}}^2\right), \\ &\bar{I}_4 = \boldsymbol{A}\cdot\bar{\boldsymbol{C}}\boldsymbol{A}, \quad \bar{I}_5 = \boldsymbol{A}\cdot\bar{\boldsymbol{C}}^2\boldsymbol{A}, \quad \bar{I}_6 = \boldsymbol{B}\cdot\bar{\boldsymbol{C}}\boldsymbol{B}, \\ &\bar{I}_7 = \boldsymbol{B}\cdot\bar{\boldsymbol{C}}^2\boldsymbol{B}, \; \bar{I}_8 = (\boldsymbol{A}\cdot\boldsymbol{B})\,\boldsymbol{A}\cdot\bar{\boldsymbol{C}}\boldsymbol{B}\end{aligned}\right\} \tag{52}$$

where $\varsigma = (\boldsymbol{A}\cdot\boldsymbol{B})^2$.

This model is capable of representing a certain class of orthotropic hyperelastic behavior with the fibric vectors $\boldsymbol{A}$ and $\boldsymbol{B}$ as input data. If, for example, we assume $\boldsymbol{B} = \boldsymbol{0}$, then the resulting energy functional can be used for a class of transversely isotropic materials introduced in [38].

References

1. Benssousan A, Lions JL, Papanicoulau G (1978) Asymptotic analysis for periodic structures. North-Holland, Amsterdam
2. Sanchez-Palencia E (1980) Non-homogeneous media and vibration theory. Springer, Berlin

3. Lions JL (1981) Some methods in mathematical analysis of systems and their control. Kexue Chubanshe Science Press and Gordon & Breach Science Pub, Beijing
4. Suquet PM (1987) Elements of homogenization theory for inelastic solid mechanics. In: Sanchez-Palencia E, Zaoui A (eds) Homogenization techniques for composite media. Springer, Berlin, pp 193–278
5. Nemat-Nasser S, Hori M (1993) Micromechanics: overall properties of heterogeneous materials. North-Holland, Amsterdam
6. Léné F, Leguillon D (1982) Homogenized constitutive law for a partially cohesive composite material. Int J Solids Struct 18:443–458
7. Devries F, Dumontet H, Duvaut G, Léné F (1989) Homogenization and damage for composite structures. Int J Numer Methods Eng 27:285–298
8. Guedes JM, Kikuchi N (1990) Preprocessing and postprocessing for materials based on the homogenization method with adaptive finite element methods. Comput Methods Appl Mech Eng 83:143–198
9. Swan CC, Cakmak AS (1994) A hardening orthotropic plasticity model for non-frictional composites: rate formulation and integration algorithm. Int J Numer Methods Eng 27:839–860
10. Ghosh S, Lee K, Moorthy S (1995) Multiple scale analysis of heterogeneous elastic structures using homogenization theory and voronoi cell finite element method. Int J Solids Struct 32:27–62
11. Fish J, Shek K, Pandheeradi M, Shephard MS (1997) Computational plasticity for composite structures based on mathematical homogenization: Theory and practice. Comput Meths Appl Mech Eng 148:53–73
12. van Rens BJE, Brekelmans WAM, Baaijens FPT (1998) Homogenization of the elastoplastic behavior of perforated plates. Comput Struct 69:537–545
13. Konke C (1995) Damage evolution in ductile materials: from micro- to macro-damage. Comput Mech 15:497–510
14. Lee K, Moorthy S, Ghosh S (1999) Multiple scale computational model for damage in composite materials. Comput Methods Appl Mech Eng 172:175–201
15. Fish J, Yu O, Shek K (1999) Computational damage mechanics for composite materials based on mathematical homogenization. Int J Numer Methods Eng 45:1657–1679
16. Terada K, Kikuchi N (1995) Nonlinear homogenization method for practical applications. In: Ghosh S, Ostoja-Starzewski M (eds) Computational methods in micromechanics, vol AMD-212/MD-62. AMSE, New York, pp 1–16
17. Smit RJM, Brekelmans WAM, Meijer HEH (1998) Prediction of the mechanical behavior of nonlinear heterogeneous systems by multi-level finite element modeling. Comput Methods Appl Mech Eng 155:181–192
18. Wieckowski Z (2000) Dual finite element methods in homogenization for elastic-plastic fibrous composite material. Int J Plast 16:199–221
19. Zheng SF, Ding K, Denda M, Weng GJ (2000) A dual homogenization and finite-element study on the in-plane local and global behavior of a nonlinear coated fiber composite. Comput Methods Appl Mech Eng 183:141–155
20. Feyel F, Chaboche JL (2000) FE^2 multiscale approach for modelling the elastoviscoplastic behaviour of long fibre SiC/Ti composite materials. Comput Methods Appl Mech Eng 183:309–330
21. Terada K, Kikuchi N (2001) A class of general algorithms for multi-scale analyses of heterogeneous media. Comput Methods Appl Mech Eng 190:5427–5464
22. Kaneko K, Terada K, Kyoya T, Kishino Y (2003) Global-local analysis of granular media in quasi-static equilibrium. Int J Solids Struct 40:4043–4069
23. Terada K, Kurumatani M (2010) Two-scale diffusion-deformation coupling model for material deterioration involving micro-crack propagation. Int J Numer Meth Eng 83:426–451
24. Yamada T (2006) Iterative algorithms for computing the averaged response of nonlinear composites under stress-controlled loadings. Int J Multiscale Comput Eng 4:475–486
25. Michel JC, Suquet P (2003) Nonuniform transformation fields analysis. Int J Solids Struct 40:6937–6955
26. Michel JC, Suquet P (2004) Computational analysis of nonlinear composite structures using the nonuniform transformation fields analysis. Comput Methods Appl Mech Eng 193:5477–5502
27. Yvonnet J, He Q-C (2007) The reduced model multiscale method (R3M) for the non-linear homogenization of hyperelastic media at finite strains. J Comput. Physics 223:341–368
28. Oskay C, Fish J (2007) Eigendeformation-based reduced order homogenization for failure analysis of heterogeneous materials. Comput Methods Appl Mech Eng 196:1216–1243
29. Matsui K, Terada K, Yuge K (2004) Two-scale finite element analysis of heterogeneous solids with periodic microstructures. Comput Struct 82:593–606
30. Takano N, Zako M, Ohnishi Y (1996) Macro-micro uncoupled homogenization procedure for microscopic nonlinear behavior analysis of composites. Mater Sci Res Int 2:81–86
31. Temizer İ, Wriggers P (2007) An adaptive method for homogenization in orthotropic nonliner elasticity. Comput Methods Appl Mech Eng 196:3409–3423
32. Watanabe I, Terada K (2005) Decoupled micro-macro analysis method for two-scale BVPs in nonlinear homogenization theory. JSCE J Appl Mech 8:277–285 (in Japanese)
33. Ren X, Chen JS, Li J, Slawson TR, Roth MJ (2011) Micro-cracks informed damage models for brittle solids. Int J Solids Struct 48:1560–1571
34. Terada K, Saiki I, Matsui K, Yamakawa Y (2003) Two-scale kinematics and linearization for simultaneous two-scale analysis of periodic heterogeneous solids at finite strain. Comput Methods Appl Mech Eng 192:3531–3563
35. Ogden RW, Saccomandi G, Sgura I (2004) Fitting hyperelastic models to experimental deta. Comput Mech 34:484–502
36. Ogden RW (1984) Non-linear elastic deformations. Dover, New York
37. ANSYS Inc. (2008) Release 11.0 Documentation for ANSYS
38. Kaliske M (2000) A formulation of elasticity and viscoelastcity for fibre reinforced material at small and finite strains. Comput Methods Appl Mech Eng 185:225–243
39. Kaliske M, Schmidt J, (2004) Nonlinear anisotropic elasticity at finite strains. In: 22nd CAD-FEM Users' Meeting 2004, International Congress on FEM Technology with ANSYS CFX & ICEM CFD Conference. Int Congress Center Dresden, Germany
40. Holzapfel GA (2000) Nonlinear solid mechanics: a continuum approach for engineering. Wiley, New York